

Using Holography and Particle Image Velocimetry to Study Particle Deposition, Re-suspension and Agglomeration

René van Hout

Abstract In this chapter two experimental imaging techniques, holography and particle image velocimetry (PIV), and their application to particle dispersed flows are discussed. Special emphasis is put on particle deposition, re-suspension and agglomeration processes. In the first two chapters the theoretical background of the techniques is presented indicating theoretical and practical limitations of both techniques. In consecutive chapters, several case studies are presented illustrating the use of both techniques. During the last decade tomographic PIV has become the leading technique in 3D flow measurements that opens up exciting new research possibilities in particle-dispersed flows. In addition, refractive index matched techniques are discussed enabling researchers to measure in detail the simultaneous coupling between finite-sized particles and turbulent flows.

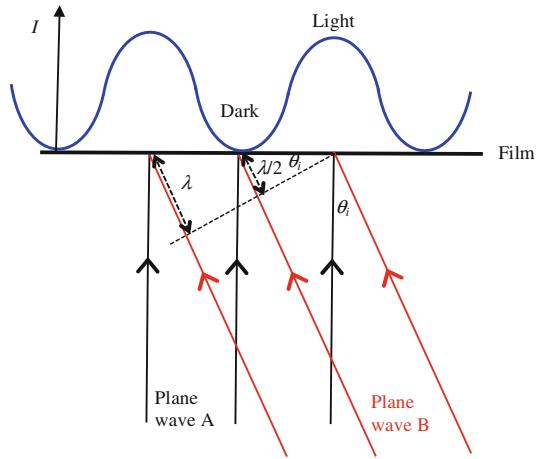
1 Holography

Holography is an imaging technique that preserves the 3-D nature of the recorded object (Collier 2013; Hariharan 1996). Gabor proposed the idea of holographic imaging in 1948 (Gabor 1948) with the aim to obtain increased resolution in electron microscopy. However, the obtained image quality was poor due to the “twin-image” problem. The breakthrough that overcame the “twin-image” problem was off-axis holography, developed in the early 1960s (Leith and Upatnieks 1962).

R. van Hout (✉)

Faculty of Mechanical Engineering, Technion – Israel Institute of Technology,
Haifa, Israel
e-mail: rene@tx.technion.ac.il

Fig. 1 Grating formed by interference between two mutually coherent plane waves A and B



1.1 Conceptual Approaches on Holography

Without further going into detail about the history and theory, holography can be explained by three different conceptual approaches (Koek 2006).

Grating formed by interference. Interference is essential to holography and without it you cannot create a hologram. It occurs when two mutually coherent plane waves of light intersect each other at an angle θ_i , resulting in a fringe pattern of bright and dark regions (see Fig. 1).

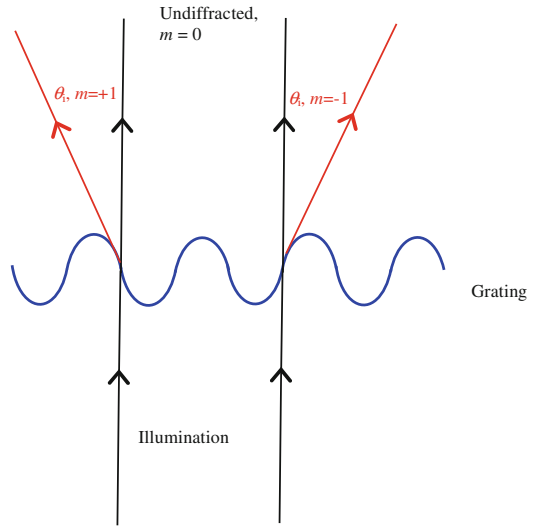
If the path length difference between the two beams is $n\lambda$ (with the integer n ranging from $n = 1$ to ∞ , and λ is the wave length) then constructive interference will occur (light region). On the other hand, if the path length difference between the two beams is $n\lambda/2$, destructive interference will occur (dark regions). The period of the resulting fringe pattern is:

$$d = \frac{\lambda}{\sin \theta_i}. \quad (1)$$

Note that Eq. (1) also puts a limit on the spatial resolution of your film as will be discussed later. If one prints the resulting intensity pattern, I , obtained in Fig. 1 on a transparent substrate, one obtains a “grating”, i.e. an object with a sinusoidally varying transmission. If this grating is illuminated, diffraction occurs and higher order beams are generated. For diffraction on a grating we can write:

$$m\lambda = d \sin \theta_m, \quad (2)$$

where m denotes the diffracted order (see Fig. 2).

Fig. 2 Diffraction at a grating

Apart from the undiffracted zero order beam (see Fig. 2), $m = 0$, the two 1st order beams ($m = \pm 1$) are likely to contain a substantial amount of light. The angle $\theta_{\pm 1}$ between the 1st order beams and the undiffracted beam is:

$$|\sin \theta_{\pm 1}| = \frac{\lambda}{d} \quad (3)$$

Noticing the resemblance between Eqs. (1) and (3), we see that “The angle under which a grating diffracts light, is exactly the angle between the two beams that formed the “grating”; This is the essence of holography.

In general, a hologram is *recorded* using a known reference wave, R , and an unknown object wave, O (see Fig. 3). Because the angle between the reference wave

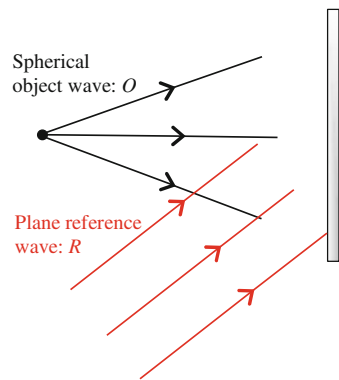
Fig. 3 Recording of hologram

Fig. 4 Reconstruction of hologram with original plane reference wave

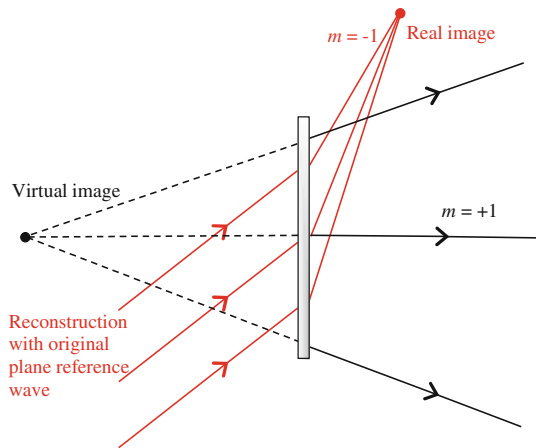
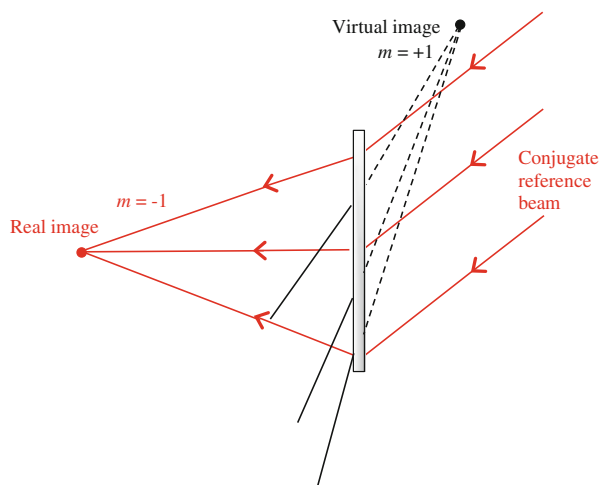


Fig. 5 Reconstruction of hologram using conjugate reference beam



and the object wave varies over the film aperture, the resulting grating will have a spatially varying period.

Upon *reconstruction* with the original plane reference wave, each local grating will diffract primarily into the first orders (see Fig. 4).

Alternatively (this is normally done), one may reconstruct the hologram with the conjugate of the original reference beam (see Fig. 5).

It can be observed that when the angle between the reference beam and the object beam is large enough, the real, virtual and reconstruction beam are spatially separated. This is called *off-axis holography*. An *in-line holography* setup is when the angle between the reference wave and the object wave is very small or zero. In that case, spatial separation is absent which may pose restrictions on its applicability. However, note that this is the setup that is used in digital holography since in order to image

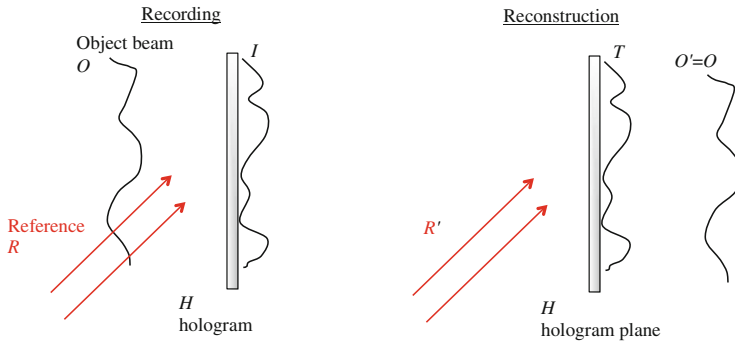


Fig. 6 Recording and reconstruction of a hologram

the fringes, and due to the limited sensor resolution, the angle θ_i needs to be small ($\theta_i < 3^\circ$, one would therefore like to have a sensor that has many and very small pixels).

So, holography enables the reconstruction of both real and virtual images of *point source objects*. However, since a physical object can be considered as an ensemble of point source objects, it is clear that a hologram can be recorded from any object, while preserving the 3D structure of the object.

Huygens' principle. An alternative way to look at holography is by means of Huygens' Principle: "Every point on a primary wave front serves as the source of spherical secondary wavelets, such that the primary wavefront at some later time is the sum of these wavelets." So Huygens' principle makes it possible to consider the hologram as a point source based wavefront regeneration device. This view is helpful when working with digital holography. With reference to Fig. 6:

Recording: A reference wave, R , falls onto the holographic film at a certain angle. As a result, it has a spatially varying phase on the film. At the same time, an object beam impinges on the film and an intensity pattern, I , is created through interference between R and O .

Reconstruction: After developing the hologram, an amplitude transmission pattern, T , is obtained, i.e. where the reference phase matches the phase of O , the hologram has a high transmission. Thus the resulting wave O' can be regarded as a collection of secondary point sources whose relative phases match those of O . As a result, wave O' will be similar to wave O .

The complex amplitude approach. This approach is the most frequent explanation encountered in textbooks. The complex object wave is given by:

$$\tilde{O}(x, y) = O(x, y)e^{-i\psi_o(x, y)}, \quad (4)$$

and the complex reference wave by:

$$\tilde{R}(x, y) = R(x, y)e^{-i\psi_r(x, y)}, \quad (5)$$

where ψ is the phase and the subscripts “o” and “r” denote “object” and “reference”, respectively; (x, y) are spatial coordinates. Upon recording a hologram, the resulting interference pattern is given by:

$$I(x, y) = \left| \tilde{O} + \tilde{R} \right|^2 = \left| \tilde{O} \right|^2 + \left| \tilde{R} \right|^2 + \tilde{O}\tilde{R}^* + \tilde{O}^*\tilde{R}, \quad (6)$$

where the superscript “*” denotes the complex conjugate. This intensity pattern will influence the transmission of the holographic film. Let’s assume that the amplitude transmission $T(x, y)$ is proportional to $I(x, y)$:

$$T(x, y) = \beta \left(\left| \tilde{O} \right|^2 + \left| \tilde{R} \right|^2 + \tilde{O}\tilde{R}^* + \tilde{O}^*\tilde{R} \right). \quad (7)$$

Now if the hologram is illuminated with a reconstruction wave $\tilde{B}(x, y)$, the complex amplitude behind the hologram is given by:

$$\tilde{E}(x, y) = \tilde{B}(x, y)\beta \left(\left| \tilde{O} \right|^2 + \left| \tilde{R} \right|^2 + \tilde{O}\tilde{R}^* + \tilde{O}^*\tilde{R} \right) = \beta\tilde{B} \left| \tilde{O} \right|^2 + \beta\tilde{B} \left| \tilde{R} \right|^2 + \beta\tilde{B}\tilde{O}\tilde{R}^* + \beta\tilde{B}\tilde{O}^*\tilde{R}, \quad (8)$$

where $\tilde{B}(x, y)$ is the original reference beam and term 3, $\beta\tilde{B}\tilde{O}\tilde{R}^* = \beta \left| \tilde{R} \right|^2 \tilde{O}$, represents the original object beam (*Real image*). Term 4, $\beta\tilde{B}\tilde{O}^*\tilde{R} = \beta \left| \tilde{R} \right|^2 \tilde{O}^*$, represents the conjugate of the original object wave (*Virtual image*). So again, we see that both a virtual and a real image may be reconstructed from the hologram.

1.2 General Requirements for Recording Holograms

An important requirement for recording holograms is that the resolution of the recording material is sufficiently high such that the intensity pattern (interference pattern of hologram) is sampled at least at the Nyquist frequency of the band-limited interference pattern (Goodman 2005; Vikram 1992). Using Eq. (1), the spatial frequency of an interference pattern formed by two overlapping beams subtending an angle θ_i is given by:

$$f = \frac{\sin \theta_i}{\lambda}, \quad (9)$$

and the minimal sampling frequency according to Nyquist is then $f_{s,\min} = 2f$. For example, let’s consider: $\lambda = 532 \text{ nm}$, $\theta_i = 45^\circ$ (off-axis recording). From this follows that $f_{s,\min} = 2\sin 45^\circ / 532 \times 10^{-9} \approx 2600 \text{ mm}^{-1}$, meaning that you would need media that can record 2600 lines/mm. This kind of resolution cannot be reached in digital recording, e.g. for a high-speed CMOS camera (Photron Ultima APX), the pixel size equals $17 \text{ }\mu\text{m}$ and typically for a green laser (Nd-Yag), $\lambda = 532 \text{ nm}$. Now

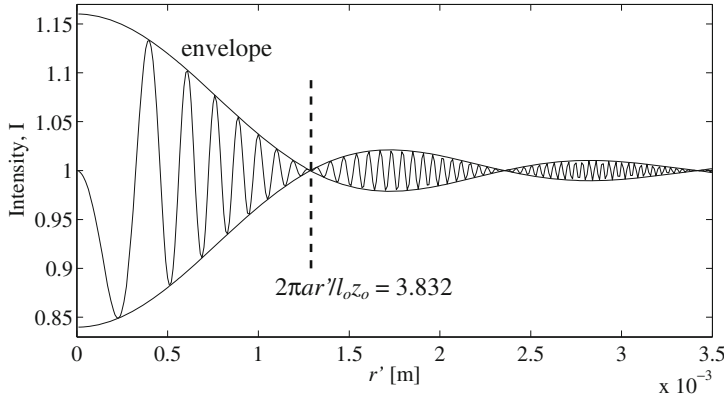


Fig. 7 Schematic diagram (not to scale) illustrating the variation of $I(r')$. The dashed vertical line corresponds to the first zero of the Bessel function

using Eq. (1), one then gets that $\sin \theta_1 = 0.0313$ or $\theta_1 \leq 2^\circ$, i.e. θ_1 is very small which basically means that for digital holography an inline setup is used.

1.3 System Design Considerations

The recorded irradiance distribution for an opaque object with a circular cross section of diameter $2a$ is given by (e.g. Vikram 1992):

$$I = 1 - \frac{2\pi m_o a^2}{\lambda_o |z_o|} \sin\left(\frac{\pi r'^2}{\lambda_o m_o |z_o|}\right) \left[\frac{2J_1(2\pi ar'/\lambda_o |z_o|)}{2\pi ar'/\lambda_o |z_o|} \right] + \left(\frac{\pi m_o a^2}{\lambda_o z_o} \right)^2 \left[\frac{2J_1(2\pi ar'/\lambda_o |z_o|)}{2\pi ar'/\lambda_o |z_o|} \right], \quad (10)$$

where r' is the radial coordinate, J_1 is the Bessel function of order one and z_o is the object distance. Thus, fine interference fringes given by the sine distribution are modulated by the $2J_1(2\pi ar'/\lambda_o |z_o|)/(2\pi ar'/\lambda_o |z_o|)$ function (see Fig. 7) that provides the diffraction pattern's envelope.

In the modulated pattern, the zeros ($I = 1$) occur at the zeros $j_{1,s}$ of the Bessel function, i.e. at $2\pi ar'/\lambda_o |z_o| = 3.832, 7.016, 10.173, 13.324$, etc. The fine fringes given by the term $\sin(\pi r'^2/\lambda_o m_o |z_o|)$ give the object distance z_o regardless of the object size. Once z_o is determined, the zeros of the modulated pattern give the object radius, a , according to:

$$a = \lambda_o z_o j_{1,s} / 2\pi r', \quad (11)$$

where r' is the radius of the ring at the s th zero. So one can actually use the recorded irradiance distribution as a means for particle sizing and position determination.

Note that in the case of digital holography, the fine fringes are not recorded and only the broad diffraction pattern is seen. This can be used for size determination if the position of the particle is known. However, note that the complex diffraction pattern does not give simple information about the object shape so it only becomes practical if the shape is known. There exists a variation of the previously described method where the coherent background is filtered and only the diffraction pattern remains (Vikram 1992) which can then be used to determine the size of objects of well-defined shape.

Film resolution requirements. First, let's have a look at the image resolution requirements and then look at the film resolution requirements (Vikram 1992).

At the time of reconstruction, if r' is the radius of the hologram aperture and the real image is observed at a distance Z_c , then according to the Raleigh resolution limit (Born and Wolf 1999), the resolved image diameter $2a$ is:

$$2 a|_{image} = 1.22\lambda_c Z_c / r', \quad (12)$$

and with $Z_c = -z_o M_c / n$ and $n = \lambda_c / \lambda_o$ leads to:

$$2 a|_{image} = 1.22\lambda_o |z_o| M_c / r', \quad (13)$$

which in the object space needs to be divided by the magnification M_c in order to give the resolvable particle diameter $2a$ as:

$$2a = 1.22\lambda_o |z_o| / r'. \quad (14)$$

Thus for a particle of diameter $2a$ to be resolved the minimum hologram radius should be $r'_{\min} = 1.22\lambda_o |z_o| / 2a$. Substituting this into the argument of the Bessel function, the first zero of the Bessel function is obtained. Thus, the central maximum needs to be recorded in order to resolve the particle. In practice, a few side lobes are normally recorded and $r'_{\min} = (1 + m)\lambda_o |z_o| / 2a$, if at least m side lobes are to be recorded.

Now let's have a look at the frequency of the fine fringes and what resolution is needed to resolve three lobes (we look at the fine fringe spacing at the edge of the lobes). For this we use the argument of the sine term in Eq. (10). Noting that the difference between the n th and the $(n + 1)$ th fringe is 2π , we obtain:

$$r'_{n+1}{}^2 - r'_n{}^2 \approx 2r' \Delta r' = 2\lambda_o m_o |z_o|, \quad (15)$$

where m_o is called the magnification from the recording setup ($m_o = 1$, for a collimated reference beam). Together with $r'_{\min} = (1 + m)\lambda_o |z_o| / 2a$, the fringe spacing is given as:

$$\Delta r' = 2am_o / (1 + m). \quad (16)$$

Equation (16) provides the minimum fringe spacing at the outer edge of the diffraction pattern or the edge of the m th lobe. If the criterion is that we want to record three lobes, we get that $\Delta r' = am_o/2$. Thus, the recording medium must resolve a spatial frequency of $2/am_o$. Accounting for the sampling theorem (Nyquist frequency) means that twice that frequency needs to be resolved, i.e. $4/am_o$. For example, if we use lensless recording without magnification, $m_o = 1$, and the particle diameter is $2a = 100 \mu\text{m}$, we get that 80 lines per millimeter or a pixelsize of $12.5 \mu\text{m}$ would do. Therefore, with a pixelsize of $17 \mu\text{m}$ we can resolve three side lobes for a particle having a diameter of $136 \mu\text{m}$. Note that if $m_o > 1$ (magnification), the film resolution can be reduced. Thus recording very small objects ($1\text{--}10 \mu\text{m}$) can be done using lenses or a divergent beam which is a lensless method that provides $m_o > 1$.

1.4 Recording Range

The minimum and maximum object distances from the recording plane are discussed here. The *minimum distance* can be as far as one far-field distance which is given by $\delta = 4a^2/\lambda_o$. For example for a $100 \mu\text{m}$ particle and a Nd:YLF laser ($\lambda_o = 527 \text{ nm}$), one far-field is about 1.9 cm. This distance is very short and is in practical situations easily fulfilled in holography of micro-objects. The *maximum recording range* is governed by the contrast of the high frequency interference fringes. If contrast is poor, the hologram will not be recorded and hence the maximum allowed subject distance becomes limited. Neglecting the last term in Eq. (10), the modulation term of the high frequency fringes, i.e. the coefficient of the sine term, is:

$$M = \frac{2\pi m_o a^2}{\lambda_o |z_o|} \frac{|2J_1(2\pi ar'/\lambda_o |z_o|)|}{2\pi ar'/\lambda_o |z_o|}. \quad (17)$$

Using the expression for r'_{min} and $m = 3$ (three side lobes) we get:

$$M = \frac{m_o |J_1(4\pi)|}{4N} \approx \frac{0.04m_o}{N}, \quad (18)$$

where N is the number of far-fields. So depending on the minimum allowable modulation M , there is a maximum allowable value of the distance. System noise, etc. will further degrade the contrast of the fringes to be recorded. Thus, in a practical experiment, the maximum allowable N can at best be determined by calibration. However, an accepted upper value of N in the collimated beam case is, $1 < N \leq 100$. Note that for small particles, the recording range becomes very limited, e.g. $2a = 5 \mu\text{m}$, $\lambda = 527 \text{ nm}$, $100 \delta = 4.7 \text{ mm}$. In such a situation, one can relay the recording plane for proper placement of the recording plane. In general, the largest particle in the subject volume should be at least one-far field away from the recording plane and the smallest one at most 100 far-fields away from the recording plane.

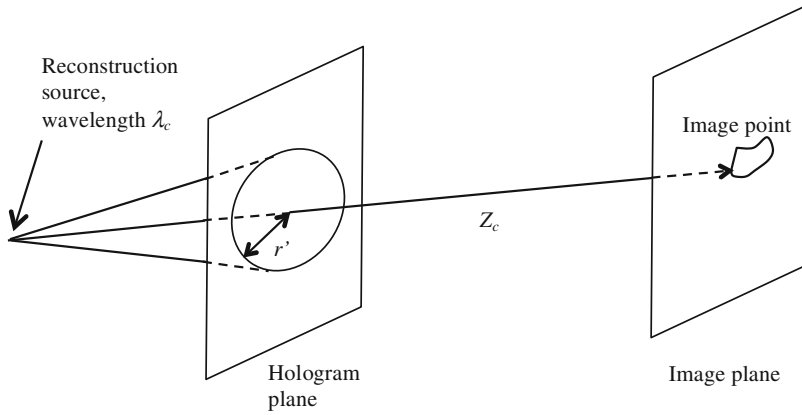


Fig. 8 Diagram for the resolution calculation due to a hologram aperture of radius r' and reconstruction wavelength λ_c

1.5 Diffraction Limited Resolution and Depth-of-Focus

The physically finite hologram aperture acts as a lens and there is a certain aperture-limited resolution. Even for a point object, there will be a certain minimum image size governed by the diffraction-limited irradiance distribution. Similarly, a point source will have a depth-of-focus uncertainty near the image (depth-of-focus). Referring to Fig. 8, the normalized diffracted irradiance due to a circular aperture of radius r' at the image plane at distance Z_c is given by the Airy distribution (Born and Wolf 1999):

$$I(R') = \left[\frac{J_1(2\pi r'R'/\lambda_c Z_c)}{2\pi r'R'/\lambda_c Z_c} \right]^2, \quad (19)$$

where R' is the radial distance in the image plane from the center of the image point. This distribution is basically the intensity diffraction pattern of the circular aperture. The radius of the central diffraction spot corresponds to $2\pi r'R'/\lambda_c Z_c \approx 3.83$ which in terms of R' turns out to be:

$$2R'_{|diffraction} \approx \frac{3.83\lambda_c Z_c}{\pi r'} \simeq \frac{1.22\lambda_c Z_c}{r'}. \quad (20)$$

Thus, even a point object will result in an image spot diameter given by Eq. (20). This spot size can be called the minimum resolvable image size. For example, for a CMOS camera Photron Ultima APX, sensor size: $17.4 \times 17.4 \text{ mm}^2$ and $\lambda_c = 527 \text{ nm}$, $Z_c = 0.2 \text{ m}$, substitution into Eq. (20) gives $2R'_{diffraction} = 7.4 \text{ } \mu\text{m}$.

Note that the spot radius is also the separation between two points that can be resolved according to the Rayleigh resolution criterion that states that two point

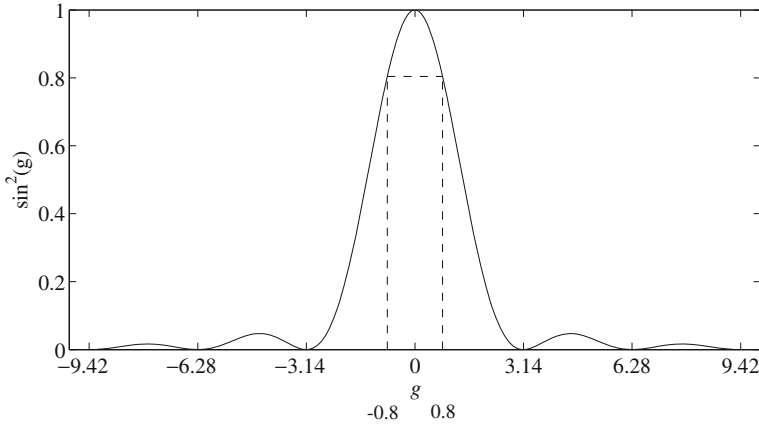


Fig. 9 Plot of the function $(\sin g)^2/g^2$ against g . The value of the function is 0.8 at $g \sim 0.8$ (Vikram 1992)

sources can be resolved when the maximum of the illumination from one source coincides with the first minimum of the illumination produced by the other.

Depth of focus: The intensity variation along the axis perpendicular to the image plane near the image is described by the normalized variation:

$$I(\Delta Z_c) = \left[\frac{\sin(\pi r'^2 \Delta Z_c / 2 \lambda_c Z_c^2)}{\pi r'^2 \Delta Z_c / 2 \lambda_c Z_c^2} \right]^2. \quad (21)$$

The function $(\sin g)^2/g^2$ is plotted in Fig. 9. If one allows for 20 % intensity loss with respect to the maximum intensity, the focal tolerance is given by:

$$\Delta Z_c|_{\text{allowable}} \sim \frac{0.8 \times 2}{\pi} \left(\frac{Z_c}{r'} \right)^2 \lambda_c \sim \pm \frac{1}{2} \left(\frac{Z_c}{r'} \right)^2 \lambda_c. \quad (22)$$

Thus the total depth of focus is $(Z_c/r')^2 \lambda_c$ which together with the diffraction spot diameter can be combined to get the well-known result that for a system that can resolve the diameter $2a$, the depth-of-focus is $4a^2/\lambda$.

1.6 Practical Considerations

Number density of micro-objects. In an inline holography setup, a commonly accepted practical limit is that a least 80 % of the light through the cross-section must be undiffracted. In the extreme case of very high number densities of micro-objects,

only a speckle pattern is formed on the recording plane. An off-axis setup allows for higher particle density, however, is not really practical for digital holography. In practice the allowable number density depends on the traversed path length through the volume where the particles reside.

Application of relay lenses. It can be advantageous to use lenses between the object and the recording plane. The main advantages of the lenses are object pre-magnification, reduced film resolution requirements, relaying the scene volume to a suitable location and even de-magnifying the scene for large micro-objects (Vikram 1992).

Object shape and fringe visibility. The in-line Fraunhofer hologram is recorded in the form of a high frequency interference pattern. The contrast of these fringes becomes low away from the center of the diffraction pattern due to the falling envelope of the pattern. Even at the center of the diffraction pattern, the contrast becomes poor if the object is very far from the recording plane. The visibility of the fringes is different for one- and two-dimensional objects. The one-dimensional case represents objects like long thin fibers whereas the circular cross-section represents bubbles, spray droplets, rain drops, pollen grains, etc. The visibility of the fringes is defined by, $V = (I_{max} - I_{min}) / (I_{max} + I_{min})$, which for circular cross-section objects is given by:

$$V(r') = \frac{8\pi N m_o \left| \frac{2J_1(2\pi a r' / \lambda_o |z_o|)}{2\pi a r' / \lambda_o |z_o|} \right|}{16N^2 + \pi^2 m_o^2 \left[\frac{2J_1(2\pi a r' / \lambda_o |z_o|)}{2\pi a r' / \lambda_o |z_o|} \right]^2}, \quad (23)$$

where, $N = \lambda_o |z_o| / (2a)^2$, is the number of far fields. Similarly, for one-dimensional opaque objects:

$$V(x') = \frac{2m_o^{1/2} N^{1/2} \left| \text{sinc}(2\pi x' / \lambda_o |z_o|) \right|}{N + m_o \text{sinc}^2(2\pi x' / \lambda_o |z_o|)}. \quad (24)$$

The visibility at the center of the hologram can be obtained by setting x' and r' to zero and the variation of the fringe visibility at the hologram center as a function of the number of far fields is plotted in Fig. 10.

The ratio of fringe visibility for a 1D and a circular object for $m_o = 1$ and large N is given by:

$$\frac{V(0)_{1D}}{V(0)_{2D \text{circ}}} \approx \frac{4N^{1/2}}{\pi} = 13 \text{ for } N = 100!!!! \quad (25)$$

So it is noted that the visibility for the 1D case is much larger than for a 2D object with the same diameter.

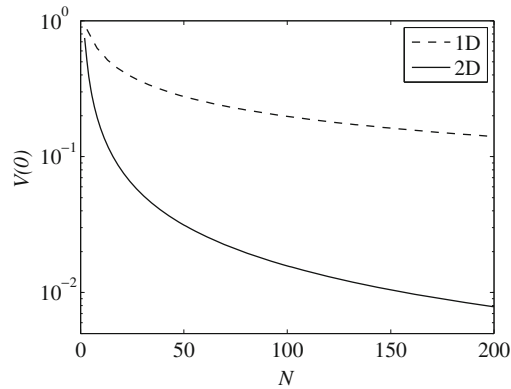


Fig. 10 Variation of fringe visibility at the center of the hologram versus the number N of far-field distances. The collimated recording beam case ($m_o = 1$) is considered here

1.7 Digital Holography

Photographic techniques have the advantage of increased spatial resolution, however, they are cumbersome in practical situations where one would like to record temporal sequences or get a quick idea of the quality of the data. Digital holography has the advantage of the relative ease of three dimensional imaging of shape, velocity and positions of dispersed particles in a volume of interest (VOI), e.g. in a turbulent

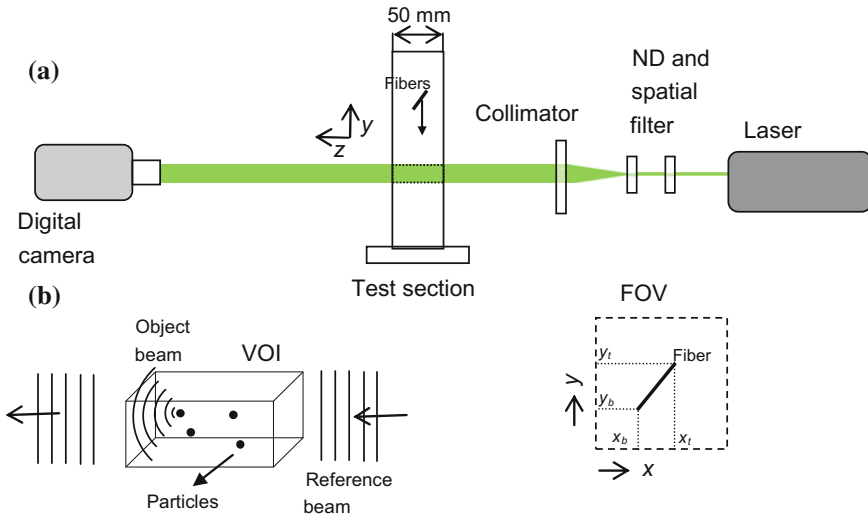


Fig. 11 Schematic layout of **a** single view, inline digital holography setup; **b** Object and reference beam in VOI; **c** Fiber coordinates in x-y plane

flow (Katz and Sheng 2010; Schnarrs and Jueptner 2005; Vikram 1992). In its most simple setup (Fig. 11), i.e. inline single-view digital holography, it consists of a laser, a light attenuator (e.g. neutral density (ND) filter), a spatial filter (focusing lens plus pinhole), a collimator and an imaging device.

One must assure spatial and temporal coherence of the laser light although the temporal coherency requirements are not very stringent in the case of an inline setup. The reference beam exiting from the collimator is led through the test section and any particles inside the VOI diffract the beam and create so-called object beams (Fig. 11b). These object beams travel further and upon reaching an acquisition device such as a CCD or CMOS sensor, they interfere with the reference beam to create an interference pattern, i.e. the hologram (Vikram 1992). The thus obtained hologram contains information on the particle position in the VOI as well as its shape. The latter can be resolved providing the spatial resolution is sufficient as was discussed previously. In case a pulsed laser or a high-speed laser and camera are used, instantaneous velocities and particle tracks can be determined.

The acquired holograms are digitally reconstructed by a 2D convolution integral of a kernel, $g(x - \zeta, y - \eta, z)$, with the optical field of the hologram, $h_r(\zeta, \eta, z = 0)$ (Katz and Sheng 2010; Milgram and Li 2002; Schnarrs and Jueptner 2005):

$$h_r(x, y, z) = \iint h_r(\zeta, \eta, z = 0) g(x - \zeta, y - \eta, z) d\zeta d\eta \quad (26)$$

where ζ and η are the in-plane coordinates at the hologram plane (located at $z = 0$) and x, y, z are the coordinates in the VOI. Thus, the hologram is reconstructed plane by plane and z acts as a parameter in the kernel. The kernel represents the diffraction of a point source and often the Kirchhoff-Fresnel approximation is used for simplicity and since it speeds up processing. Using the convolution theorem, Eq. (26) can be easily evaluated in the frequency domain:

$$h_r(x, y, z) = \mathcal{F}^{-1} [\mathcal{F}(h_r) \mathcal{F}(g)] \quad (27)$$

where \mathcal{F} represents a Fourier transform.

One of the inherent disadvantages of single-view holography is the in-depth (z) position inaccuracy (depth-of-focus, Fig. 11). As discussed previously, the in-depth position of the particle scales as $\sim 4a^2/\lambda$ (Vikram 1992), e.g. for $2a = 100 \mu\text{m}$ and $\lambda = 532 \text{ nm}$, the particle remains visible in the reconstructions over a distance of 18.8 mm or $376a$, clearly problematic if one wants to estimate the particle's 3D position. In order to more accurately determine the particle's in-depth position, different methods have been proposed to determine the in-focus-position from holograms (Choi and Lee 2009, 2011; Fournier et al. 2004; Langehanenberg et al. 2008; Murata and Yasuda 2000; Pan and Meng 2003; Yang et al. 2005), based on:

- (i) Minimum sum of intensities: pixel intensities, $I(x, y)$, are summed over a masked, cropped reconstruction containing only the particle on a uniform background (Murata and Yasuda 2000) and the minimum or maximum sum of intensities corresponds to the in-focus position.

- (ii) Maximum intensity standard deviation: based on increased gray scale, intensity contrast as the hologram is reconstructed closer to the in-focus position corresponding to maximum intensity standard deviation (Pan and Meng 2003).
- (iii) Maximum rms of intensity gradients: like method (ii), based on increased gray scale, intensity contrast as the hologram is reconstructed closer to the in-focus position, i.e. maximum rms of intensity gradients (Choi and Lee 2009; Langehanen et al. 2008), calculated by the “Prewitt” operator (Jain 1989).

These methods are all applied on small, cropped hologram reconstructions that contain the considered particle. An example of the detection of the in-focus position of a fiber (Nylon, $dtex = 0.9$, diameter $D_f = 10 \mu\text{m}$, length $L_f = 0.5 \text{ mm}$) and a

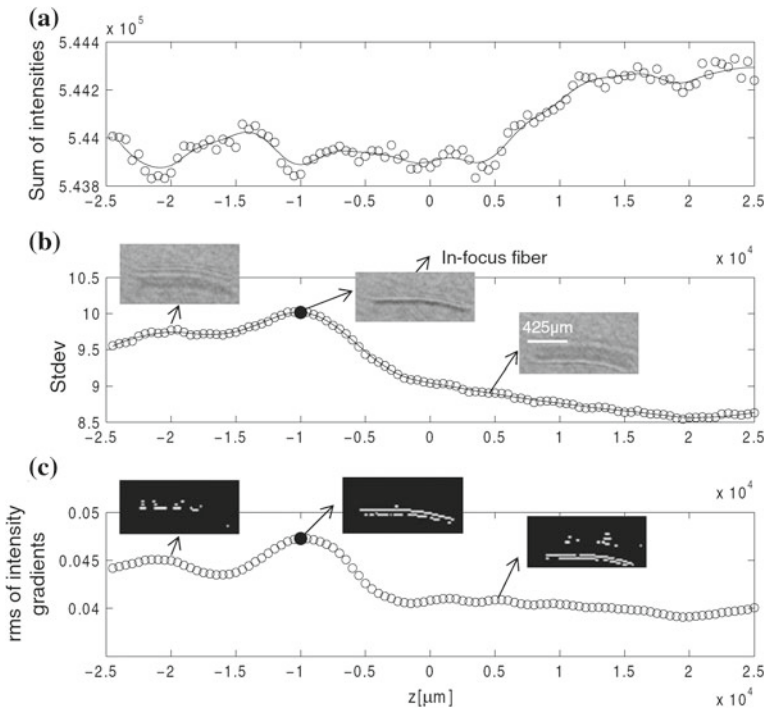


Fig. 12 Detection of the in-focus position of fibers using **a** Sum of intensities, **b** Intensity standard deviation, **c** rms value of intensity gradients (“Prewitt” operator). Reconstructions at $\Delta z = 500 \mu\text{m}$. Inserts in **(b)** are reconstructions and those in **(c)** are the corresponding edge detected ones. (van Hout et al. 2013)

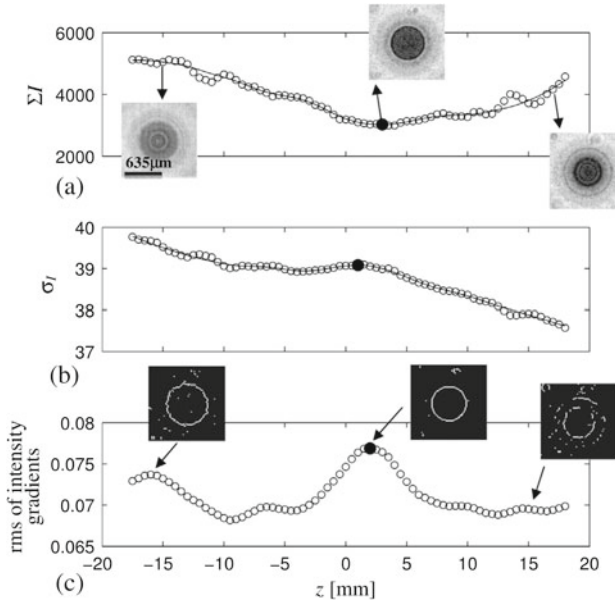


Fig. 13 Comparison between three different methods for detecting the in-focus position of a spherical bead having a diameter of $500 \mu\text{m}$. **a** Sum of intensities, **b** Intensity standard deviation, **c** rms value of intensity gradients (“Prewitt” operator). Reconstructions at $\Delta z = 500 \mu\text{m}$. Inserts in **(b)** are reconstructions and those in **(c)** are the corresponding edge detected ones (Rabencov and van Hout 2014)

spherical bead ($2a \approx 580 \mu\text{m}$) using these three methods are shown in Figs. 12 and 13, respectively. In both cases, the spatial measurement resolution was $17 \mu\text{m}/\text{pix}$, more than sufficient for the bead but insufficient to resolve the fiber diameter. The inserts in Figs. 12b and 13a are examples of reconstructions at different z , while those in Figs. 12c and 13c are the corresponding edge detected images. The black dots indicate the in-focus position of the fiber or bead as determined by the different methods. It can be seen that the sum of intensities method does not provide a clear global minimum for the fiber while for the bead this is the case for the maximum intensity standard deviation.

If one can acquire cinematographic data, particles can be tracked in space and time, and their orientations may be determined. An example of an in-focus tracked sequence of a single fiber settling in water and beads of diameter $\sim 0.5 \text{ mm}$ in a turbulent water channel as well as reconstructions at different in-depth positions are displayed in Fig. 14. The fiber was located at approximately 60 cm (or more than 2700 far fields based on fiber diameter, $N = D_f^2/\lambda = 22 \text{ mm}$) from the camera’s sensor but still clearly comes into focus as the holograms are reconstructed at different in-depth positions. On the other hand, for the beads one far field equals, $N = (0.5 \times 10^{-3})^2/527 \times 10^{-9} = 0.47 \text{ m}$, and the recording medium was positioned just a little more than one far-field away. The spatial measurement resolution ($17 \mu\text{m}/\text{pix}$) is

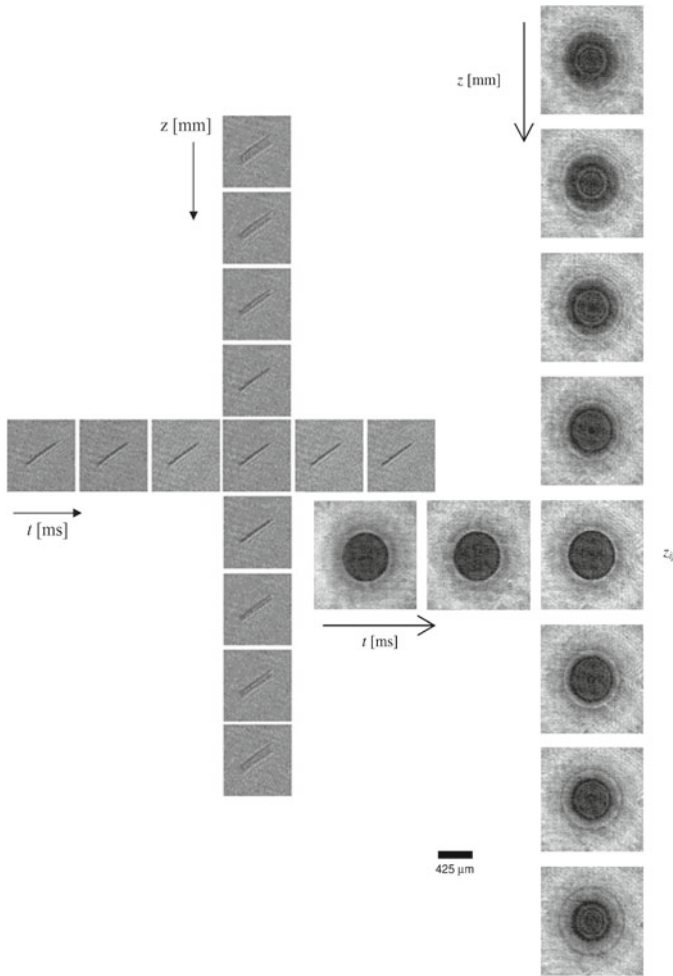


Fig. 14 Example of in-focus reconstruction at different times (*row*) and in-depth reconstructions at different z locations (*column*). **a** Fiber ($d_{\text{tex}} = 0.9$) settling in water, $\Delta t = 20$ ms, $\Delta z = 1$ mm; **b** Bead ($d = 0.5$ mm), $\Delta t = 1$ ms, $\Delta z = 5$ mm

clearly insufficient to resolve the fiber diameter ($\langle D_f \rangle = 10.81 \mu\text{m}$); however, it is suited to accurately ($\sim 5\%$ error) measure the fiber length ($\langle L_f \rangle = 0.476$ mm). In order to increase the spatial resolution, magnifying lenses can be used (e.g. long working distance microscopic lenses). However, note that when the particle is small compared to the wavelength of the light, any shape information is lost (Vikram 1992) and the particles will act as point scatterers.

If the aim is also to resolve the orientation of anisotropic particles, additional views are needed. For example, single view, inline digital holography applied to dilute fiber suspension flows only resolves the fiber orientation projected onto the plane

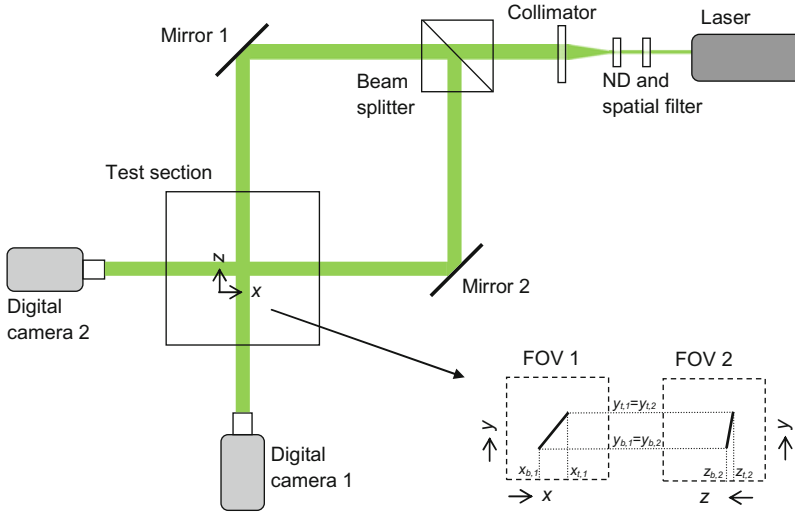


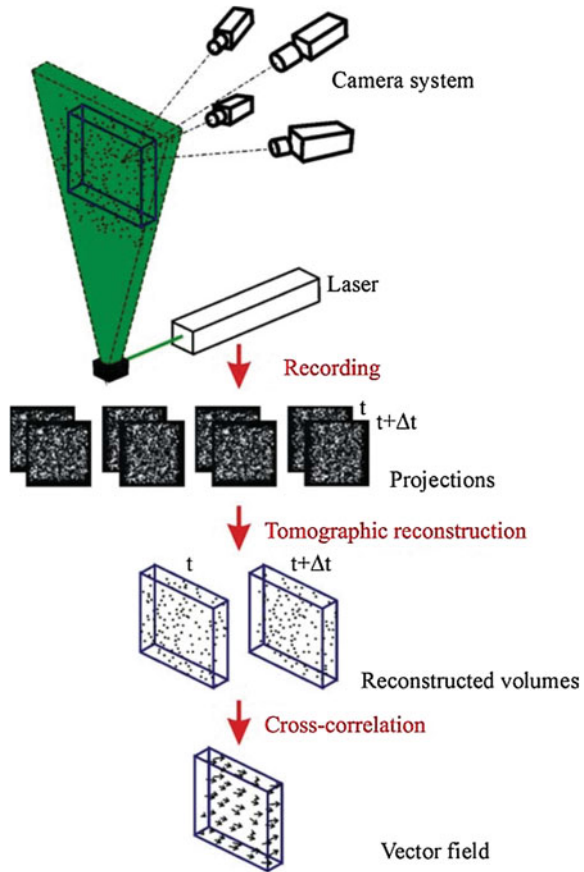
Fig. 15 Schematic of **a** orthogonal, double view, inline digital holography and **b** fiber coordinates in two orthogonal views

perpendicular to the camera (Fig. 11c) and does not resolve the 3D fiber orientation. In order to do so, two perpendicular views are needed as indicated in the schematic layout in Fig. 15. The disadvantage of this type of setup is that two cameras are needed although orthogonal view setups have been established using one camera and a 45° tilted mirror. The two-orthogonal views now provide an accurate estimate of the fiber's 3D position and orientation in the VOI as illustrated in Fig. 15b. The fiber's top and bottom coordinates are indicated by the subscripts “t” and “b”, respectively; cameras 1 and 2 are indicated by subscripts “1” and “2”, respectively. The accurate in-plane x, y (top and bottom) fiber coordinates of camera 1 are complemented by the in-plane y, z coordinates imaged by camera 2 such that the inherent in-depth inaccuracy does not play a role. Note that $y_{t,1} = y_{t,2}$ and $y_{b,1} = y_{b,2}$, which facilitates matching between the two orthogonal views.

2 Tomographic Particle Image Velocimetry

The instantaneous measurement of the 3D velocity field is of great interest to fluid mechanics research as it enables one to reveal the complete topology of unsteady coherent flow structures. Moreover, 3D measurements are relevant for those situations where the flow does not exhibit specific symmetry planes or axes such as turbulent flows that are intrinsically 3D and their full description requires measurement techniques that are able to capture the instantaneous 3D structure, the complete stress tensor and the vorticity vector (Scarano 2013; Westerweel et al. 2012).

Fig. 16 Schematic of working principle of tomographic PIV (Elsinga et al. 2006)



2.1 Working Principle of Tomographic PIV

The working principle of tomographic-PIV is schematically represented in Fig. 16 (Elsinga et al. 2006). Tracer particles immersed in the flow are illuminated by a pulsed light source within a 3D region of space. The scattered light pattern is recorded simultaneously from several viewing directions using CCD or CMOS cameras. In order to focus correctly from an oblique viewing angle, the Scheimpflug condition (similar as in stereoscopic-PIV) between the image plane, lens plane and the mid-object-plane is applied. Furthermore, the particles across the depth of the entire volume need to be imaged in focus, which is obtained by setting a proper $f_{\#}$. The 3D particle distribution (the object) is reconstructed as a 3D light intensity distribution from its projections on the CCD arrays. The reconstruction is an inverse problem and its solution is not straightforward since it is in general underdetermined, i.e. many different 3D objects can result in the same set of projections. After reconstruction, the particle displacement (hence velocity) within a chosen interrogation volume is

then obtained by the 3D cross-correlation of the reconstructed particle distribution at the two exposures.

The relation between image (projection) coordinates and the physical space (the reconstruction volume) is established by a calibration procedure common to stereo-PIV. Each camera records images of a calibration target at several positions in depth throughout the volume. The calibration procedure returns the viewing directions and field of view. The tomographic reconstruction relies on accurate triangulation of the views from the different cameras. The requirement for a correct reconstruction of a particle tracer from its images sets the accuracy for the calibration to a fraction of the particle image size. Therefore, a technique for the a-posteriori correction for the system misalignment, “self-calibration”, significantly improves the accuracy of the reconstruction (Wieneke 2008). The mapping from physical space to the image coordinate system can be performed by means of either the camera pinhole model or by a third-order polynomial in x and y (Elsinga et al. 2006).

Volume illumination. Laser systems in use for planar PIV have commonly been used for tomographic volume illumination. The latter is obtained in a somehow simpler way than for planar PIV, because a region of typically 1 cm thickness is obtained and most Nd:YAG lasers have a beam exit diameter of comparable size. Therefore the optical components for volume illumination can be reduced to a minimum of a single cylindrical diverging lens. When the required thickness is larger than the laser beam exit diameter, a beam expander may be of practical use.

The common denominator to illumination systems for tomo-PIV is the use of knife-edge filters to cut the light intensity beyond the nominal thickness of the measurement volume. Any light recorded onto the imagers that originates from regions outside the reconstructed volume will be included in the reconstructed object, increasing the noise in the reconstructed signal.

Tomographic imaging. The quality of tomographic PIV measurements depends upon the imaging system design. The recorded particle images should be in focus and with a sufficient intensity such that they can be easily separated from the background intensity. Several parameters govern the quality of the imaging process: the camera sensitivity (quantum efficiency) and sensor pixel size Δ_{pix} , the optical magnification M , the settings of the objectives and the solid angle θ subtended among the viewing directions. Popular setups consist of placing four cameras along the vertices of a pyramid or placing the cameras in a cross configuration (Fig. 17). The latter setup has the advantage of an easier setting of the lens-tilt adapter (the lens plane rotates vertically or horizontally). Experiments were also conducted with all cameras along a line with an arc-like system, with the result that the outer cameras must be set to a large viewing angle (Fig. 17).

Optical and digital depth-of-focus. It is crucial that the particles are imaged in focus ensuring that the sensor area covered by particle images is minimized for a given amount of particles. The condition to be respected is that the focal depth δz should be larger or equal to the depth of the illuminated volume ΔZ . According to diffraction optics the optical focal depth is given by:

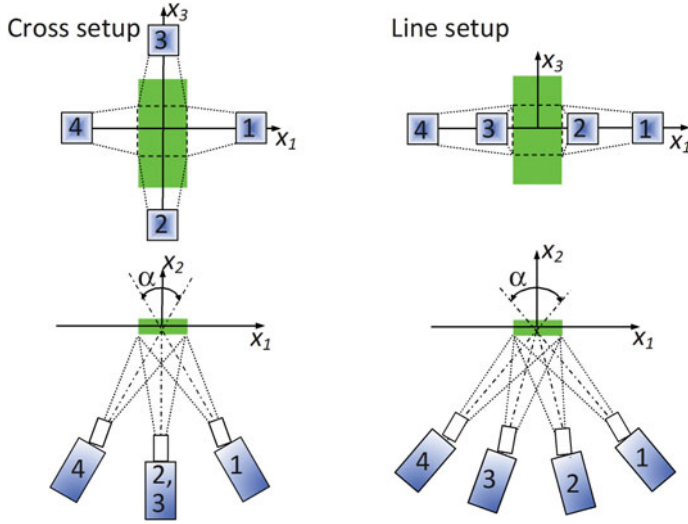


Fig. 17 Schematic of possible cross and line setup imaging configurations (4 cameras) for tomographic PIV systems

$$\delta z = 4.88 \lambda f_{\#}^2 \left(1 + \frac{1}{M} \right)^2, \quad (28)$$

where λ is the wavelength of light and $f_{\#}$ the numerical aperture (“ f -number”: ratio of the lens’s focal length to the diameter of the entrance pupil). The diffraction limited image diameter of a particle placed inside the depth of focus is (Raffel et al. 2007):

$$d_{diff} = 2.44 f_{\#} (M + 1) \lambda. \quad (29)$$

In PIV, this minimum image diameter d_{diff} will only be obtained when recording small particles—of the order of a few microns—at small magnifications. For larger particles and/or larger magnifications, the influence of geometric imaging becomes more and more dominant. Equation (28) provides the means to estimate the $f_{\#}$ in order to get the VOI in focus. In practice, particles will be slightly blurred due to imaging aberrations and non-perfect alignment etc. (see Scarano 2013), and the actual $f_{\#}$ will be determined during the experimental setup.

Seeding density. The concentration of particle tracers within the measurement volume ultimately determines the spatial resolution of the measurement. The number of particles within an interrogation box (IB) required to perform a robust cross-correlation analysis varies between 5 and 10, considering that the phenomenon of particle loss-of-pairs is negligible for 3D particle motion analysis.

The concentration of particle tracers in the measurement domain is limited by the maximum image source density that the tomographic reconstruction can accu-

rately handle. Elsinga et al. (2006) showed that a four-camera system accurately reconstructs images with a seeding density of 0.05 ppp (particles per pixel). The value depends mostly on the number of cameras, the pixel normalized particle image diameter and the quality of the imaging process (particle image peak intensity).

2.2 Tomographic Reconstruction Algorithms

There are several possible tomographic reconstruction algorithms. One of the most popular ones is MART (multiplicative algebraic reconstruction technique). Algebraic methods iteratively solve a set of linear equations modeling the imaging system. In the present approach the measurement volume containing the particle distribution (the object) is discretized as a 3D array of cubic voxel elements in (X, Y, Z) (in tomography referred to as the basis functions) with intensity $E(X, Y, Z)$.

A cubic voxel element has a uniform non-zero value inside and zero outside and its size is usually chosen comparable to that of a pixel, because particle images need to be properly discretized in the object as it is done in the images. Moreover, the interrogation by cross-correlation can be easily extended from a pixel to a voxel based object. Then the projection of the light intensity distribution $E(X, Y, Z)$ onto an image pixel (x_i, y_i) returns the pixel intensity $I(x_i, y_i)$ (known from the recorded images), which is written as a linear equation:

$$\sum_{j \in N_i} w_{i,j} E(X_j, Y_j, Z_j) = I(x_i, y_i), \quad (30)$$

where N_i indicates the voxels intercepted or in the neighborhood of the line of sight corresponding to the i th pixel (x_i, y_i) (shaded voxels in Fig. 18). The weighting coefficient $w_{i,j}$ describes the contribution of the j th voxel with intensity $E(X_j, Y_j, Z_j)$ to the pixel intensity $I(x_i, y_i)$ and is calculated as the intersecting volume between the voxel and the line of sight (having the cross sectional area of the pixel) normalized with the voxel volume. The coefficients depend on the relative size of a voxel to a pixel and the distance between the voxel center and the line of sight (distance d in Fig. 18). Note that $0 \leq w_{i,j} \leq 1$ for all entries $w_{i,j}$ in the 2D array W and that W is very sparse, since a line of sight intersects with only a small part of the total volume. A range of algebraic tomographic reconstruction algorithms is available to solve these equations. However, due to the nature of the system, the problem is underdetermined and the calculation may converge to different solutions, which implies that these algorithms solve the set of equations of Eq. (28) under different optimization criteria. The algorithm most adopted for tomographic-PIV (tomo-PIV) is MART described in the following.

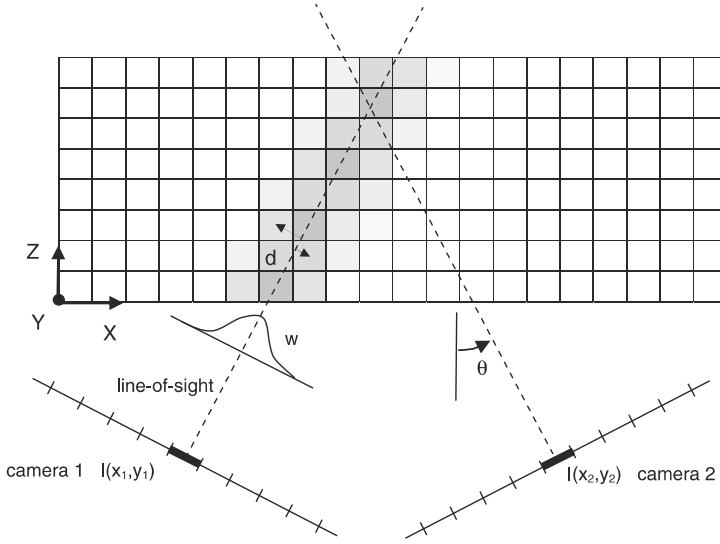


Fig. 18 Representations of the imaging model used for tomographic reconstruction. In this *top*-view, the image plane is depicted as a line of pixel elements and the measurement volume is a 2D array of voxels. The *gray* level indicates the value of the weighting coefficient ($w_{i,j}$) in each of the voxels with respect to the pixels $I(x_1, y_1)$ (Elsinga et al. 2006)

MART algorithm: Starting from a suitable initial guess ($E(X, Y, Z)^0$ is uniform), the object $E(X, Y, Z)$ is updated in each full iteration as:

1. for each pixel in each camera i :
2. for each voxel j :

$$E(X_j, Y_j, Z_j)^{k+1} = E(X_j, Y_j, Z_j)^k \left(I(x_i, y_i) / \sum_{j \in N_i} w_{i,j} E(X_j, Y_j, Z_j)^k \right)^{\mu w_{i,j}}$$

end loop 2

end loop 1.

Here, μ is a scalar relaxation parameter, which for MART must be ≤ 1 . In MART the magnitude of the update is determined by the ratio of the measured pixel intensity I with the projection of the current object $\sum w_{i,j} E(X_j, Y_j, Z_j)$. The exponent again ensures that only the elements in $E(X, Y, Z)$ affecting the i th pixel are updated. Furthermore, the multiplicative MART scheme requires that E and I are definite positive. The multiplicative MART scheme behaves as AND-operator, i.e. non-zero intensity are obtained only at locations where a particle appears in all recordings.

Elsinga et al. (2006) performed a parametric study using synthetic images and the reconstruction quality, Q , defined as the ratio between reconstructed particle volume and actual particle volume is depicted in Fig. 19. The diagrams show clear trends that provide the experimentalist with a first indication of the optimum experimental arrangement and the limitations of the system. The effect of

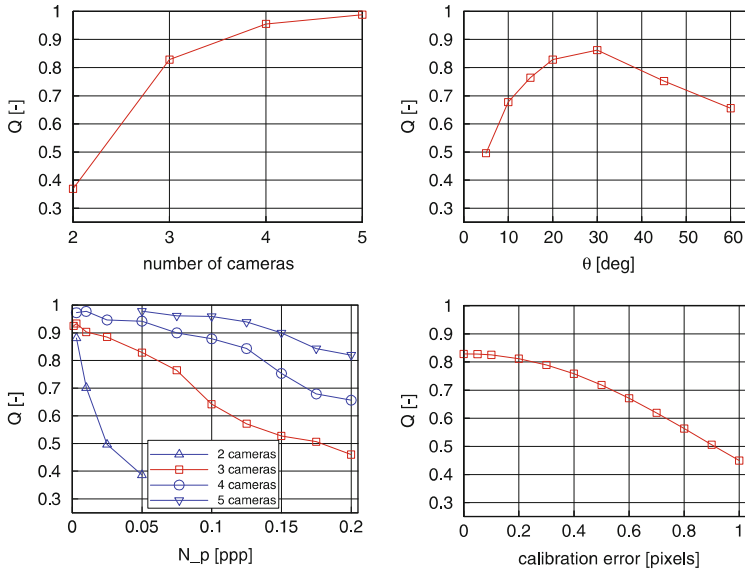


Fig. 19 Reconstruction quality Q as a function of **a** the number of cameras, **b** viewing angle, **c** particle density and **d** calibration accuracy. (Taken from Elsinga et al. 2006)

the number of cameras is clear: adding a camera gives additional information on the object, which increases reconstruction accuracy. A 2-camera system ($\theta = -20^\circ$ and 20°) is largely insufficient, whereas Q rapidly increases going to three and four cameras ($\theta = -20^\circ, 0^\circ, 20^\circ$ and 40°) and approaches unity with five cameras ($\theta = -40^\circ, -20^\circ, 0^\circ, 20^\circ$ and 40°). The viewing angles are changed maintaining the symmetric camera arrangement. The angle indicated in Fig. 19 is the angle between the outer cameras and the z -axis. The graph shows an optimum near 30° . For smaller angles the depth resolution decreases resulting in elongation of the reconstructed-particle in depth. For larger angles the intercepted length of the line-of-sight increases, which causes a larger number of particles to be formed with respect to those actually present in the illuminated volume. Such extra particles are referred to as “ghost particles” (Maas et al. 1993). “Ghost particles” are a problem of ambiguity, which increases with the number of particles, the particle diameter and the length of the line of sight in the volume. The latter increases with the viewing angle in the present configuration, hence the increase in ghost particles. The configurations returning an optimum have a viewing angle in the range of 15 – 45° .

Figure 20 illustrates the mechanism of ghost particle formation. The simplified case of a 2D object is considered: when two cameras record a set of two particles, four possible particles are the solution of the reconstruction algorithm. This problem is referred to as ghost particles (Elsinga et al. 2006; Maas et al. 1993). Introducing a third viewing direction completely solves the ambiguity. An accurate reconstruction is still possible at higher seeding density as long as most particles are projected

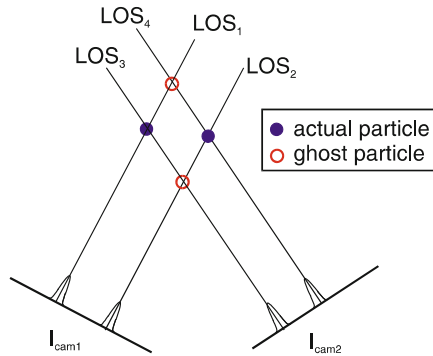


Fig. 20 Formation of ghost particles in a 2-camera setup. LOS denotes “line of sight” (Elsinga et al. 2011)

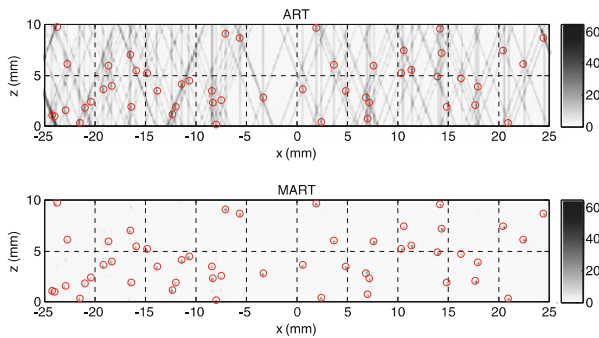


Fig. 21 Particle field reconstructed using ART (*top*) and the MART (*bottom*). Actual particle positions are indicated by circles. Gray level represents intensity level. (Elsinga et al. 2006)

onto well distinct images, as shown in Fig. 21. The solution obtained by iterative ART (Algebraic Reconstruction Techniques) and MART calculation is illustrated in Fig. 21.

The intensity reconstruction by the ART exhibits peaks at intersections of the lines of sight where particles are detected. However, the object intensity initially distributed along the entire lines of sight intercepting particles is not entirely eliminated with further iterations. The object reconstruction by the MART follows a similar pattern at the first iteration. The multiplicative algorithm eliminates the spurious intensity along lines of sight with the subsequent iterations. As a result a significantly higher accuracy is gained in comparison to the ART method. Nevertheless, at high seeding density, also the reconstruction obtained from the MART suffers from a lower contrast due to the increased number of ghost particles.

From this simple simulation the importance of iteratively updating the intensity became clear. The reconstruction accuracy as a function of MART iterations increases significantly until five iterations and after that further iterations bring only marginal improvements and the process can be stopped.

2.3 Vortex Identification and Data Validation

The main advantage of a 3D measurement compared to the planar one is the simultaneous evaluation of the velocity vector and the velocity gradient tensor within a measurement domain extending over the three coordinate directions (Scarano 2013). As a result, the organization of turbulent motions can be inspected less ambiguously making use of Galilean invariant vortex detection methods (Kolář 2007).

Q-criterion: Hunt et al. (1988) identify vortices of an incompressible flow as connected fluid regions with a positive second invariant of the velocity gradient tensor taking into account all components:

$$Q \equiv \frac{1}{2} (\|\boldsymbol{\Omega}\|^2 - \|\mathbf{S}\|^2) > 0, \quad (31)$$

where $\boldsymbol{\Omega}$ and \mathbf{S} result from the decomposition of the velocity gradient tensor into anti-symmetric and symmetric parts, respectively. Thus, it detects the regions where the vorticity magnitude prevails over the strain-rate magnitude. Note that the norm (or absolute tensor value) $\|\mathbf{G}\|$ of any tensor \mathbf{G} is defined by $\|\mathbf{G}\| = [\text{tr}(\mathbf{G}\mathbf{G}^T)]^{1/2}$. In addition, the pressure in the vortex region is required to be lower than the ambient pressure. Since the very first applications of tomographic PIV, the organization of vortical structures such as hairpins in turbulent boundary layers has been visualized by the *Q*-criterion (Elsinga and Westerweel 2010).

Δ -criterion: Chong et al. (1990) define vortices as the regions in which the eigenvalues of ∇u are complex (a pair of complex-conjugate eigenvalues occurs) and the streamline pattern is spiraling or closed in a local reference frame moving with the point. For incompressible fluids this requirement reads as:

$$\Delta = \left(\frac{Q}{3}\right)^3 + \left(\frac{R}{2}\right)^2 > 0, \quad (32)$$

where Q (Eq. (29)) and $R \equiv \text{Det}(\nabla u)$ are the invariants of ∇u . Q and R play a key role in the reduced (due to incompressibility) characteristic equation for the eigen-values λ of ∇u : $\lambda^3 + Q\lambda - R = 0$ (Chong et al. 1990).

λ_2 criterion: The approach of Jeong and Hussain (1995) is formulated on dynamic considerations, namely on the search for a pressure minimum across the vortex. By taking the gradient of the Navier–Stokes equations and by decomposing it into symmetric and antisymmetric parts they derive the well-known vorticity transport equation and the strain-rate transport equation. The latter reads

$$\frac{DS_{ij}}{Dt} - \nu S_{ij,kk} + \Omega_{ik}\Omega_{kj} + S_{ik}S_{kj} = -\frac{1}{\rho}p_{,ij}, \quad (33)$$

where the pressure Hessian $p_{,ij}$ (the subscript comma denotes differentiation) contains information on local pressure extrema. The occurrence of a local pressure minimum

in a plane across the vortex requires two positive eigenvalues of the tensor $p_{,ij}$. By removing the unsteady irrotational straining and viscous effects from the strain rate transport Eq. (31) one yields the vortex-identification criterion for incompressible fluids in terms of two negative eigenvalues of $S^2 + \Omega^2$. The existence of a local pressure minimum is neither a sufficient nor a necessary condition for the presence of a vortex in general, and the two removed terms from Eq. (31) are found to be the main cause of this inaccuracy. Finally, a vortex is defined as a connected fluid region with two negative eigenvalues of $S^2 + \Omega^2$. Since the tensor $S^2 + \Omega^2$ is symmetric, it has real eigenvalues only. If these eigenvalues are ordered as follows, $\lambda_1 \geq \lambda_2 \geq \lambda_3$, the vortex identification criterion is equivalent to the resulting condition $\lambda_2 < 0$.

The validity and accuracy of 3D data can be scrutinized a-posteriori, invoking a number of physical principles. The first one involves the local mass conservation, dictating that for an incompressible flow the velocity field must be solenoidal (divergence-free):

$$\nabla \cdot \vec{V} = 0. \quad (34)$$

This approach was proven effective to estimate the uncertainty of the measured velocity spatial derivatives (Liu and Katz 2006; Scarano and Poelma 2009). Another option: when the vorticity and velocity distribution are measured with sufficient temporal resolution, the accuracy of the measurement can be scrutinized through the consistency of the data with respect to the vorticity equation (for incompressible flow):

$$\frac{D\vec{\omega}}{Dt} = (\vec{\omega} \cdot \vec{\nabla}) \vec{u} + \nu \nabla^2 \vec{\omega}, \quad (35)$$

where D/Dt is the material derivative. The first term on the right hand side describes the stretching or tilting of vorticity due to the flow velocity gradients.

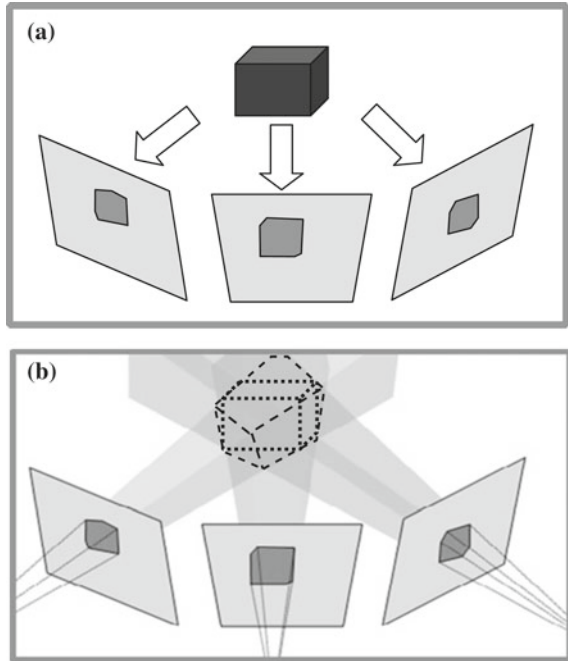
2.4 The Application of Tomo-PIV to Particle-Laden Flows

In order to apply tomo-PIV to particle-laden flows special care must be taken to identify and mask the particles.

Visual Hull technique (silhouette-based back-projection). The visual hull technique, which employs multiple camera views of a single object, detects the silhouette of the object seen by each camera (see Fig. 22a). Silhouettes are then extruded to create cone-like volumes that intersect to form the object's visual hull (see Fig. 22b). This technique results in a reconstructed object (dashed lines in Fig. 22b) that is consistently larger in volume than the original object (dotted lines in Fig. 22b). Increasing the number of projected images obviously leads to a more accurate reconstruction.

The visual hull technique has two predominant limitations that prevent it from reconstructing the object perfectly: (1) a limited number of cameras and (2) no ability to resolve concavities. With only four cameras, the problem is underdetermined, and thus, perfect reconstruction of the object is improbable. Nonetheless, the visual hull

Fig. 22 Visual hull technique. **a** Projected silhouettes of an object in individual image planes, **b** Back-projection for object reconstruction. Note that the cube (*dotted lines*) in (**b**) is smaller than the intersection of back-projected volumes (*dashed lines*). (Adhikari and Longmire 2012)



of the object appears similar to the shape of the actual object and thus gives a good estimate of the location of the object within the field of view.

3 Particle-Laden Flows, Practical Aspects in Experiments

3.1 PIV: Separation Between Flow Tracers and Particles

In order to process particle-laden PIV images, the essential, first step is separating the flow tracers from the (large) particles. Different possibilities have been explored such as distinguishing tracers and particles based on color, e.g., by using fluorescent tracers. Another method that has been used extensively is based on the size difference between suspended particles and the tracers.

The importance of masking particles in the original PIV images is illustrated in the following. The effect of masking nylon fibers on the obtained flow field was quantified by comparing the obtained PIV velocity vector (bold quantity) field without masking, \mathbf{U}_{PIV} , to that obtained with a mask, $\mathbf{U}_{PIV,mask}$. The application of the mask is illustrated in Fig. 23a. Note that the applied mask is increased in size by dilatation in order to remove any reflections in the neighborhood of the filter. Multiplication of the original PIV image by the mask results in a masked image containing only the tracers. An example of the normalized difference between the obtained velocity

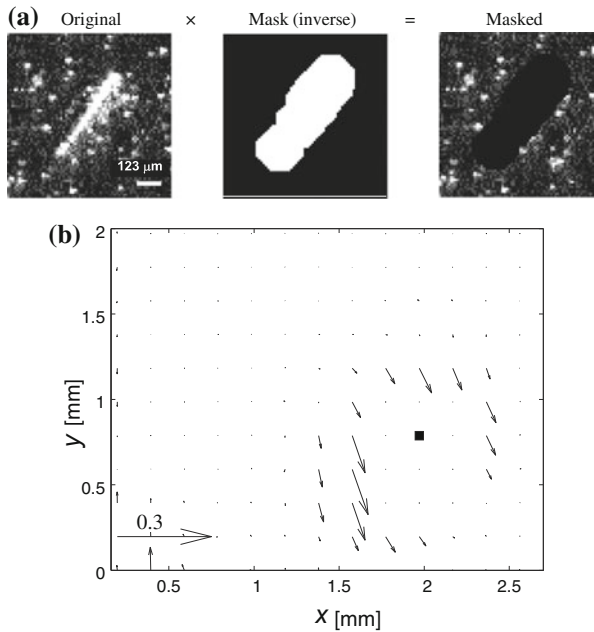


Fig. 23 Effect of applying a mask on the velocity field in the vicinity of a fiber. **a** Mask generation, **b** difference between PIV vectors without mask and masked PIV, $(U_{PIV} - U_{PIV,mask})/|U_{PIV}|$. Black square in (b) indicates fiber center (van Hout et al. 2013)

fields, $(U_{PIV} - U_{PIV,mask})/|U_{PIV}|$, is shown in Fig. 23b. As expected, the velocity field is only affected close to the fiber with differences up to 15% of the instantaneous local velocity magnitude. Although these velocity differences are relatively small they become significant when one determines gradients in the vicinity of the fibers. It is therefore essential to carefully mask any particles if one wants to study the flow field characteristics in the vicinity of them.

Size/intensity based. Small tracers can be removed by applying a local median filter (Gonzalez and Woods 2002) that replaces the value of each pixel by the median value of a region in its neighborhood. Thus, large particles can be removed by applying a median filter to the raw PIV images and subtracting the resulting image (“the mask”) from the original one, leaving only the tracers. The optimal size of the median filter depends on the imaged size of the PIV tracers. Isolated tracers whose imaged area is less than $n^2/2$, can be removed by an $n \times n$ median filter (Gonzalez and Woods 2002), where n is the median filter size. The procedure is illustrated in Figs. 24 and 25 for nylon fibres and polystyrene beads, respectively. In order to mask the fibers, a 5×5 median filter was used while typical tracer particle sizes were 4–5 pixels. Note that this median filter size is a compromise between “masking efficiency” and “erosion” of the fiber’s optical signature, i.e., increasing the median filter size would also remove parts of the fiber.

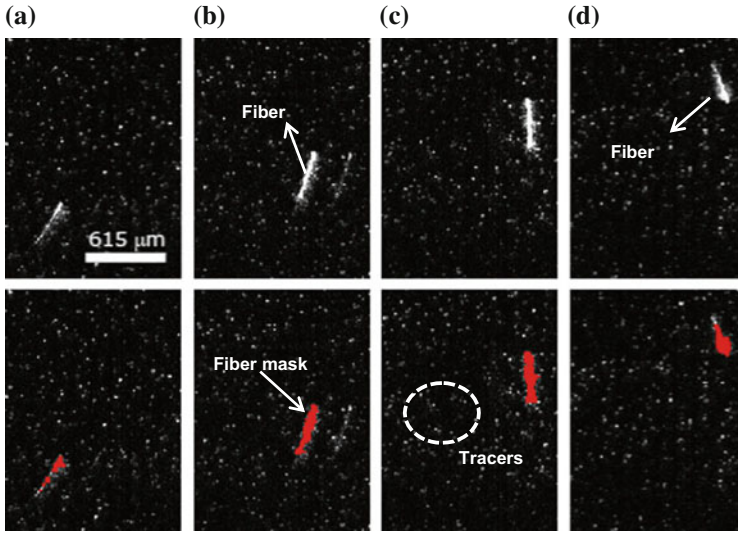


Fig. 24 Sequence of cropped PIV images including a fiber acquired in near homogeneous isotropic turbulence at 3 kHz. Time difference between images is 2.33 ms. *Upper row* original PIV images; *lower row* masked parts of the fiber depicted in red

The procedure is illustrated in Fig. 24 for a Nylon fiber characterized by $dtex = 1.7$, where $dtex$ represents the mass of the fiber in grams per 10,000 m. The fibers were released in near homogeneous, isotropic air turbulence (HIT) (Sabban and van Hout 2011). The images were captured at 3 kHz using a single camera, planar PIV setup. Due to the highly three-dimensional flow, the fibers display a strong out-of-plane motion and reside only for a short time inside the laser sheet while continuously changing their orientation. Note that due to the out-of-plane motion and changing orientation, the “intensity signature” of the fiber continuously changes, limiting perfect separation of tracers and fibers. Median filtered images were binarized and subsequently subtracted from the original PIV images. The results are depicted in the lower row of Fig. 24 where the red blobs indicate the parts that were masked. In this particular case, it can be observed that the fibers are quite well removed from the PIV images mostly leaving only the tracers. Note that the chosen threshold for binarization depends on the acquired image quality and is often manually determined for each data set. In general, it is advisable to choose a relatively low threshold value so that the mask removes most of the fiber as well as any reflections in its vicinity. An in-depth investigation on the effect of different intensity contrast enhancement techniques (Gonzalez and Woods 2002) has not been performed. However, since separation between fibers and tracers is based on their size difference and the imaged fibers often suffer from reflections and intensity saturation in their vicinity, it is not expected that intensity adjustment will significantly improve neither separation nor determination of fiber geometrical features.

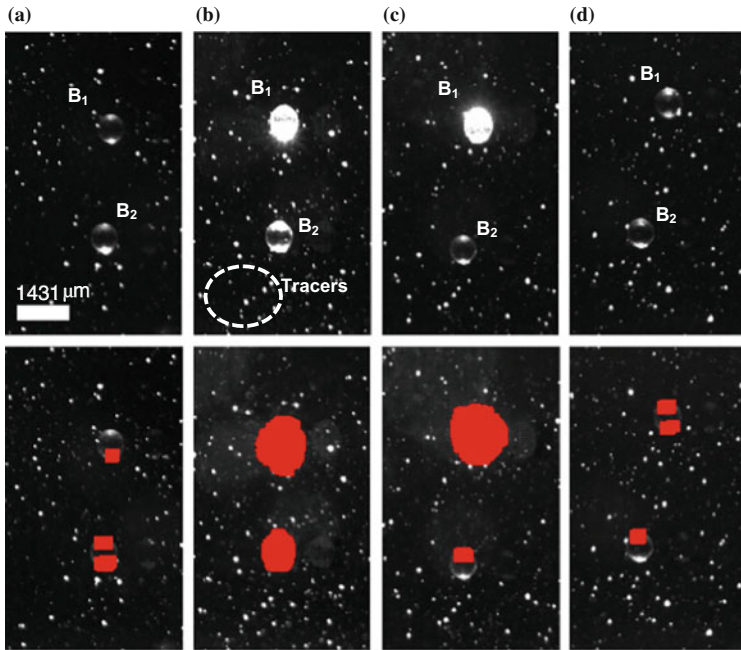


Fig. 25 Sequence of cropped PIV images showing the removal of beads using a median filter technique. $\Delta t = 15$ ms, original data set acquired at 1 kHz. *Upper row* original cropped PIV images. *Lower row* PIV images with masked beads (indicated by *red blobs*) (van Hout et al. 2013)

Problems with reflections or intensity signature of particles. An example for which the above described procedure works less well is shown in Fig. 25. Here, polystyrene beads (diameter $d_p = 583 \mu\text{m} \pm 14.4 \mu\text{m}$) are suspended in a turbulent water channel flow (van Hout 2011, 2013). The “median filter” method usually works well when the size difference between tracers and particles is substantial. However, it is problematic when the particles are not exactly in focus or when their “signature” in the PIV images is not fully bright as shown in Fig. 25. The upper row shows a sequence displayed at $\Delta t = 15$ ms (original data taken at 1 kHz) of two beads, B_1 and B_2 , that are tracked across the FOV. Both tracers as well as beads can be easily detected especially in the original high-speed sequence (not shown here). However, the partially transparent bead’s “signature” changes significantly during its passage through the FOV from fully bright (Fig. 25b, c) to two dots (Fig. 25a, d) on the top and bottom of the beads. The second row in Fig. 25 displays the corresponding subtracted images (applying a median filter and dilatation). Again the red blobs indicate the masked areas. It is immediately clear that this method is unable to accurately remove the beads from the original PIV images. Therefore, the remaining parts of the beads, e.g. in Fig. 25a, c, and d (lower row), will affect the consecutive PIV analysis in a way similar to that shown in the beginning of this chapter.

One of the main reasons for applying high-speed techniques is to be able to resolve both the particle as well as the flow field characteristics both in time and in space. However, as noted previously this may be difficult due to the changing signature of the particle, e.g. due to slightly different light reflection/refraction as a result of out-of-plane motion, spatial lighting inhomogeneity or particle rotation (for irregularly shaped particles). When the measurements are performed at sufficient temporal resolution (e.g., of the same order as the particle response time), these particles can be successfully tracked by applying a local cross-correlation technique

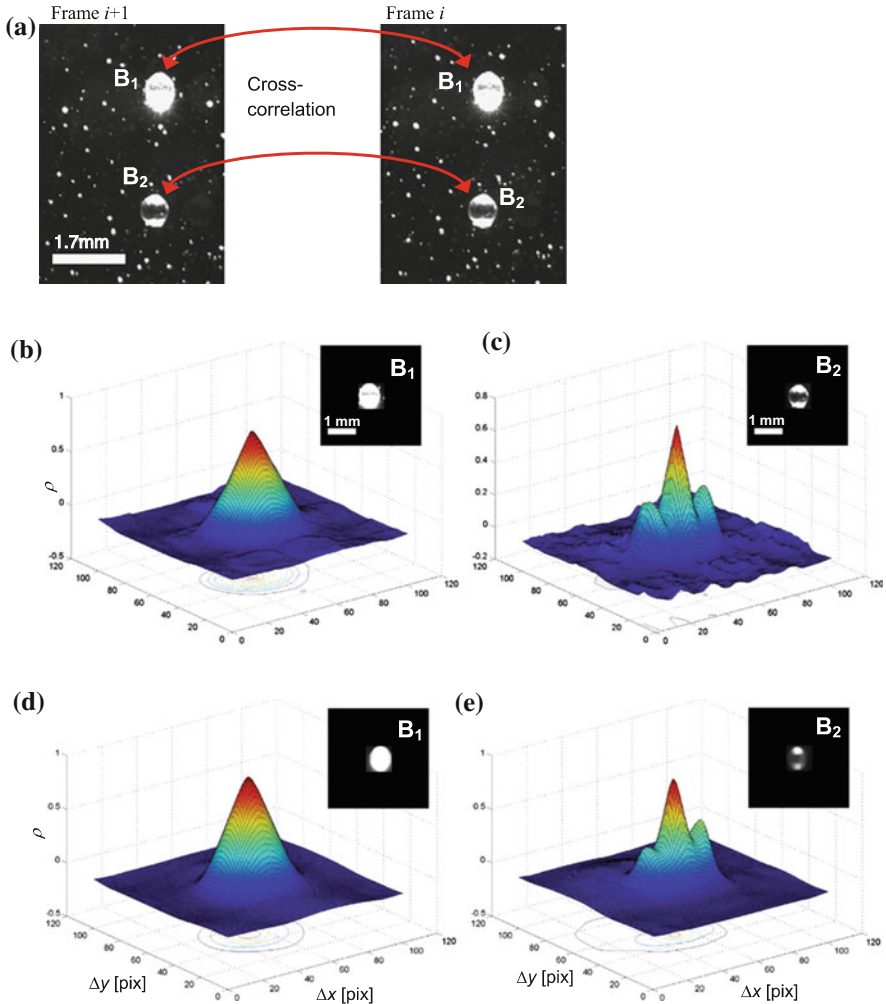


Fig. 26 Example of tracking procedure for beads B_1 and B_2 . **a** Sequence of two cropped PIV images, $\Delta t = 1$ ms; Cross-correlation coefficient maps **(b), c** without applying a median filter and **d, e** after applying a median filter. Inserts show cropped images used for cross-correlation

as illustrated in Fig. 26 for spherical beads and fibers, respectively. This procedure consists of the following steps. First, a particle is identified upon entering the FOV, and its instantaneous velocity is estimated from two subsequent instances. Identification upon entering the flow field can be automated for example by taking advantage of the size difference between tracers and particles. Once the instantaneous velocity of a specific particle has been determined, its centroid is shifted accordingly, and the PIV image is cropped around the predicted particle position in the next frame. Examples of two consecutive frames containing beads B_1 and B_2 (data acquired at 1 kHz) are displayed in Fig. 26. In comparison with Fig. 25 in which the time difference between frames was 15 ms, it can be observed that the bead's intensity signature does not change significantly within 1 ms. Therefore, the cropped images in frames i and $i + 1$ containing a single bead at their center can be cross correlated in order to determine the bead displacement. Examples of the cross-correlation function, $\rho(\Delta x, \Delta y)$, are displayed in Fig. 26b–e together with examples of the cropped images containing a bead at their center. Note that tracers in the vicinity of the particle can substantially affect the peak of the cross-correlation coefficient and care must be taken to remove them, e.g., by applying a median filter or blanking them out away from the bead (providing the bead's size is approximately known). While the cross-correlation function of B_1 (Fig. 26b, d) displays a clear single peak, the “double dotted” bead, B_2 (Fig. 26c, e), exhibits three peaks, one near the center of the cropped image and two peaks, one at each side. Applying a median filter (Fig. 26d, e) improved the tracking in most instances by reducing spurious noise mainly due to tracers that remained visible near the beads. Subpixel accuracy can be obtained by standard techniques such as centroid determination or three-point Gaussian fitting techniques applied to the correlation maps (Raffel et al. 2007). This method has been successfully applied to track partially transparent polystyrene beads in a turbulent water channel flow by van Hout (2011, 2013) when the bead's signature significantly changed.

3.2 Holography: “Silhouette” Imaging

As discussed in Sect. 1, holography images the particle's silhouette, however without having to worry too much about the depth of focus as would be the case in back-light photography. In the following, two case studies will be discussed. The first discusses a single-view, in-line digital holography setup concerning the break-up of pollen clumps upon release from a flower. The second one discusses a two-orthogonal view, inline digital holography setup that is able to measure the 3D orientation of nylon fibers in a turbulent flow.

Case study: Disintegration of particle clumps using single inline holographic cinematography. Pollen clump release, trajectories and possible breakup were measured using high-speed, digital inline holographic cinematography, schematically shown in Fig. 27. The system consisted of a high speed, pulsed Nd:YLF laser (Crystalaser, 523 nm, 10 μ J at 10 kHz), filtering optics and a high-speed CMOS camera (Photron Ultima APX, 1024 \times 1024 pixels at 2 kHz, 17 \times 17 μ m² pixels). The

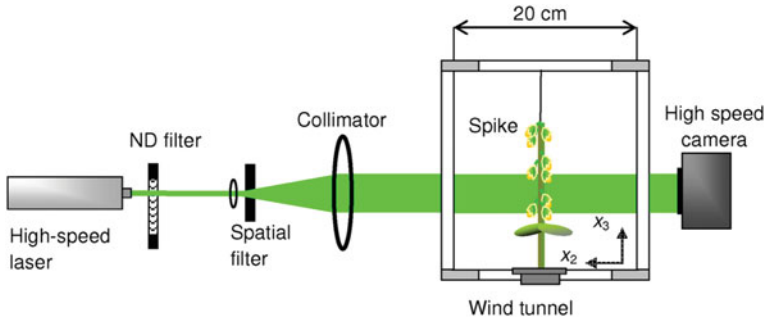
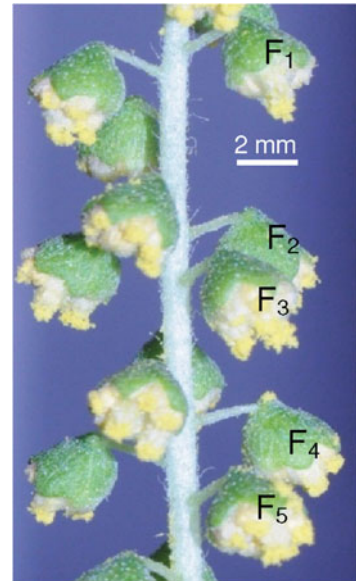


Fig. 27 Schematic layout of the high speed, digital inline holographic cinematography system (not to scale). (Sabban et al. 2012)

Fig. 28 Side view photograph of a ragweed (*A. confertiflora*) spike mounted in the wind tunnel. (Sabban et al. 2012)



optics consisted of a neutral density (ND) filter, a spatial filter (aspherical focusing lens and $10\ \mu\text{m}$ pinhole) and a spherical collimator lens (focal length, $f = 200\ \text{mm}$). The collimated laser beam passed through the test section where it was partially diffracted by any obstacles such as pollen and the ragweed staminate flowers. As a result, interference patterns (holograms) of the diffracted ‘object’ beam with the ‘reference’ beam were recorded (Vikram 1992) at the camera’s sensor plane (see Fig. 27). The recordings were lensless and had a spatial resolution of $17\ \mu\text{m}/\text{pixel}$. The resulting volume of interest (VOI) was $17 \times 17 \times 200\ \text{mm}^3$ centered in the x_2 direction on the spike.

A side view (x_2 direction) of the ragweed spike is presented in Fig. 28 where the different involucres or cups, each containing multiple flowers (Bianchi et al. 1959),

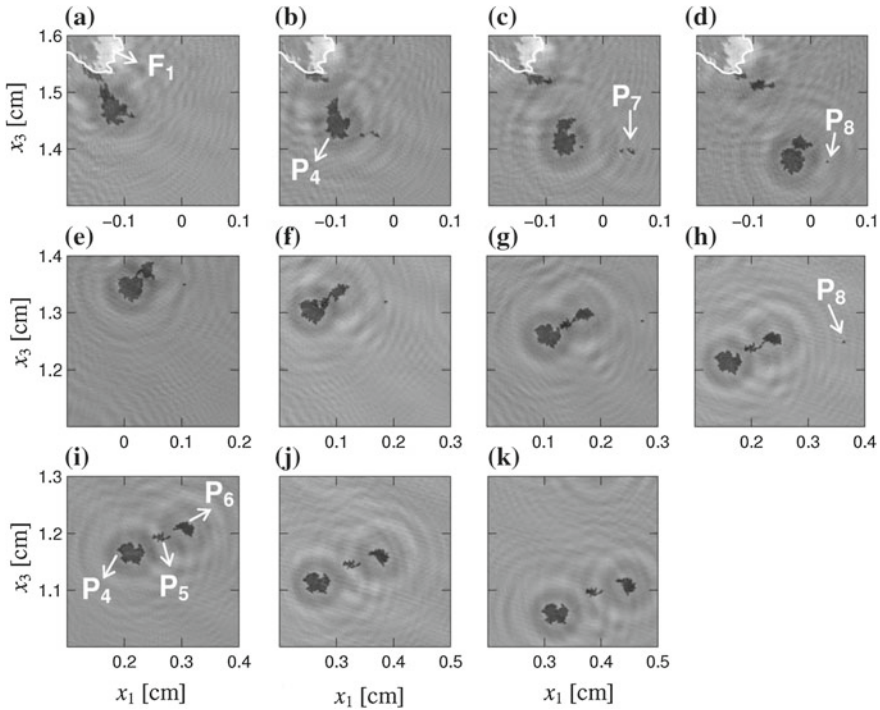


Fig. 29 Sequence of pollen clump release and breakup. $\Delta t = 0.002$ s, $U_\infty = 1.5$ m/s. The white solid curves indicate the borders of cups and staminate flowers. (Sabban et al. 2012)

seen in the holographic FOV's are indicated by F_1 to F_5 . Several of the flowers have dehisced and pollen is exposed to the air flow.

Figure 29 shows the release of a large amount of pollen by the ragweed spike. A large clump P_4 ($\sim 7,185$ pollen) is released from flower F_1 . Initially two small clumps, P_7 (~ 185 pollen) and P_8 (~ 13 pollen), break loose from P_4 and are advected away from F_1 . As P_4 settles further, it becomes distorted, stretched (Fig. 29e–g) and finally breaks up into three parts, P_4 to P_6 in Fig. 29i. Note that P_5 (~ 425 pollen) and P_6 ($\sim 1,598$ pollen) are still connected by a thin strand of pollen in Fig. 29h.

Case study: Rotation and translation of fibers. Measurements of nylon fiber rotation and translation were performed in a $40 \times 40 \times 40$ cm³ turbulence chamber (Hwang and Eaton 2004; Sabban and van Hout 2011) having transparent acrylic windows to ensure optical access (see Fig. 30). Near homogeneous, isotropic air turbulence was generated by eight woofers mounted on the corners of the chamber. The reader is referred to Sabban and van Hout (2011) for further details. Nylon fibres ($L_f = 0.5$ mm, $D_f = 15$ μ m) were released from the top of the chamber using a custom-made particle dispenser that consisted of a small cylindrical container.

3D fibre orientational and translational dynamics were measured using a two orthogonal view, digital inline holographic cinematography system (van Hout 2013).

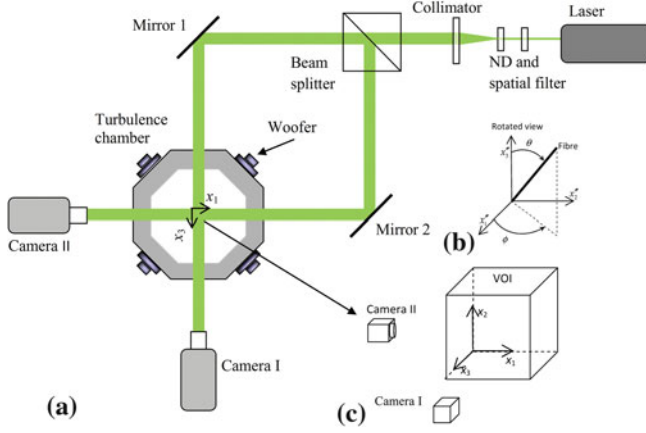


Fig. 30 Schematic layout of **a** the experimental facility and digital holography system (not to scale) and coordinate systems attached to **b** fiber, **c** VOI

The system schematically depicted in Fig. 30, comprised a high speed laser (Crysta-laser, $10 \mu\text{J}/\text{pulse}$ at 10 kHz) two high-speed, lensless cameras (Photron UltimaAPX, 1024×1024 pixels at 2 kHz , $17 \mu\text{m}/\text{pixel}$), a spatial filter (aspherical focusing lens and $10 \mu\text{m}$ pinhole), collimating lens ($f = 200 \text{ mm}$), a beam splitter (54 mm cube) and two mirrors to direct the laser beam to the cameras. The volume of interest (VOI) was a cube of approximately $17 \times 17 \times 17 \text{ mm}^3$ where the two collimated beams intersected. One of the coordinate systems, x'_i , moved with the fibre and its origin at the start of a fibre track was taken at the most left point in the field of views (FOV) of cameras I and II as shown in Fig. 30. Note that the common coordinate, x_2 , in both cameras' FOV's was used to "match" fibres in both camera views. The fibre angles ϕ and θ were defined in a spherical coordinate system and are given by:

$$\phi = \tan^{-1} \left(\frac{x'_2}{x'_1} \right), \quad (36)$$

and

$$\theta = \cos^{-1} \left(\frac{x'_3}{L} \right). \quad (37)$$

The fibre unit orientation vector, \mathbf{p} , is then defined in terms of its orientation angles, ϕ and θ , as (Olson 2001):

$$\mathbf{p} = \begin{bmatrix} \cos \phi \sin \theta \\ \sin \phi \sin \theta \\ \cos \theta \end{bmatrix} \begin{bmatrix} \hat{j} \\ \hat{k} \\ \hat{l} \end{bmatrix}, \quad (38)$$

where $\hat{j}, \hat{k}, \hat{l}$ are unit vectors in the x'_i ($i = 1, 2, 3$) direction, respectively. The orientational fibre velocity is then given by:

$$\dot{\mathbf{p}} = \dot{\phi} \sin \theta \hat{\phi} + \dot{\theta} \hat{\theta}, \quad (39)$$

where $\hat{\phi} = [-\sin \phi; \cos \phi; 0]$ and $\hat{\theta} = [\cos \phi \cos \theta; \sin \phi \cos \theta; -\sin \theta]$ are the corresponding unit vectors and $\dot{\phi}$ and $\dot{\theta}$ are the angular fibre velocities.

3.3 Measurement of Rotation and Translation of Refractive Indexed Matched Particles in Turbulent Flows Using PIV and PTV

A promising technique that has been used to study the interaction between relatively large (several millimeters, Taylor scale range) particles and turbulent flows is the use of refractive index matched particles “seeded” with flow tracers. In this way, both the flow tracers in the flow as well as those “embedded” in the particles are imaged enabling the determination of both particle translation/rotation as well as resolving the surrounding flow field. Bellani et al. (2012) reported stereo-PIV measurements of spherical and ellipsoidal refractive indexed matched, near-neutrally buoyant particles in near-isotropic homogeneous turbulence. An example of a PIV measurement that images both flow tracers as well as tracers embedded in refractive index matched particles is shown in Fig. 31.

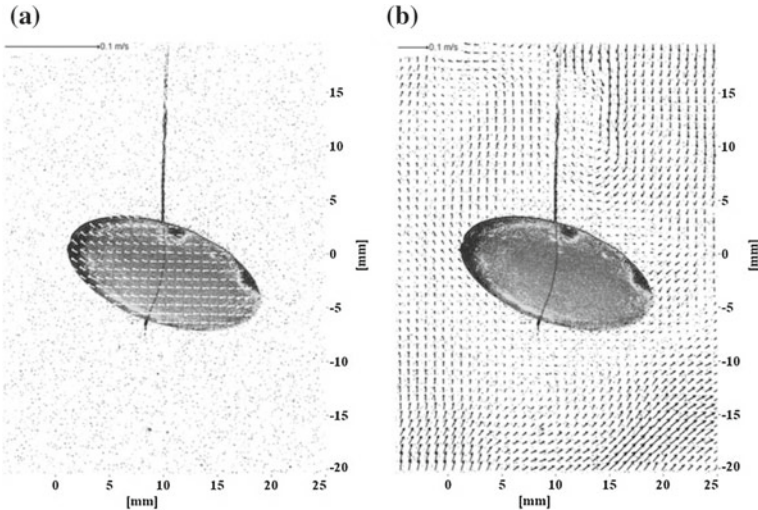


Fig. 31 PIV showing **a** solid-body motion of points within a moving macro particle and **b** turbulent flow in surrounding water. (Byron and Variano 2013)

Klein et al. (2013) used a similar technique but now performed volumetric measurements. They report simultaneous measurements of the trajectories, the translation and the rotation in three dimensions of finite-size inertial particles together with the turbulent flow. The flow field is analyzed by tracking the temporal evolution of small embedded, fluorescent tracer particles. The inertial particles consist of a super-absorbent polymer that renders them index and density matched with water and thus invisible. Inserting tracer particles into the polymer at various locations marks the inertial particles. Translation and rotation, as well as the flow field around the particle are recovered dynamically from the analysis of the marker and tracer particle trajectories.

To measure the rotation of the inertial particles, Klein et al. (2013) used the center position together with the trajectories of the markers around the center of the sphere by applying an algorithm first introduced by (Kabsch 1976). This algorithm seeks the optimal rotation matrix, \mathbf{U} , between two sets of points by minimizing the root mean square of their separation. In order to apply Kabsch's algorithm, first the sphere center position must be determined. This can be done using the sphere equation as outlined by Klein et al. (2013). The center position \mathbf{x}_c and radius R_p of the inertial particle are entirely defined by the sphere equation:

$$(x_i - x_c)^2 + (y_i - y_c)^2 + (z_i - z_c)^2 = R_p^2, \quad (40)$$

where $(x_i; y_i; z_i)$ are the i th marker's 3D-coordinates. For each permutation of four markers this can be written as a linear system (see Klein et al. 2013), that is then solved $n!/(4!(n-4)!)$ times, where n is the total number of markers. Note that the obtained sphere center positions may be weighted averaged, the weight determined by the distribution of the tracer particles on the sphere (i.e. agglomerations of tracer particles will less accurately determine the sphere center in comparison to homogeneously distributed ones).

Once the center positions of the spheres are known, Kabsch's algorithm (Kabsch 1976) may be applied. This algorithm seeks the optimal rotation matrix \mathbf{U} between two sets of points by minimizing the root mean square of their separation (see Klein et al. 2013). Considering two sets x and y of N paired points that have the same centroid at the origin, a 3×3 unitary matrix \mathbf{U} is looked for that aligns x best with y . This is achieved by minimizing the root mean square:

$$D = \left[\frac{1}{N} \sum_{j=1}^N (Ux_i - y_i)^2 \right]^{1/2}, \quad (41)$$

or after rewriting, the following needs to be maximized:

$$\sum_{i=1}^N Ux_i y_i = \text{Tr} (Y^T U X) = \text{Tr} ((XY^T) U). \quad (42)$$

Using singular value decomposition (SVD), the 3×3 matrix XY^T can be rewritten as $XY^T = VSW^T$. V and W^T are orthogonal matrices of the left and right eigenvectors of XY^T and S is a diagonal 3×3 matrix containing the eigenvalues $s_1 \geq s_2 \geq s_3$. After applying some additional constraints (see Klein et al. 2013), the optimal rotation matrix is given by:

$$U = W \begin{pmatrix} 1 & 0 & 0 \\ 0 & 1 & 0 \\ 0 & 0 & d \end{pmatrix} V^T, \quad (43)$$

where $d = \text{sign}(\det(XY^T))$. Thus one can apply this algorithm in the following way: (i) determine sphere center positions, (ii) construct matrices of tracer particle locations with respect to the center position of the sphere: $N \times 3$ matrices $X_{ni} = x_{ni}(t) - x_{c,i}(t)$ and $Y_{ni} = x_{ni}(t + \Delta t) - x_{c,i}(t + \Delta t)$, where x_{ni} are the position components of the n th marker trajectory that existed at times t and $t + \Delta t$. For each time step, the covariance matrix $C = XY^T$, is computed, its SVD $C = VSW^T$ and the sign of its determinant $d = \text{sign}(\det(C))$. Finally, Eq. (43) is applied to obtain the optimal rotation matrix U . From the rotation matrix, one can extract the rotation vector or the Euler angles and compute the rotation rate of the inertial particle ω .

4 Experiments on Particle and Flow Dynamics in Wall-Bounded Turbulent Flows

4.1 Near-Wall, Turbulent Flow Structures

It has been known since long that wall-bounded turbulent flows are populated by coherent flow structures that are largely responsible for heat and mass transfer (Elsinga and Westerweel 2010; Robinson 1991). More recently, the advent of tomographic particle image velocimetry has enabled the visualization of the different topologies of the coherent structures residing in a turbulent boundary layer even in a high Reynolds number, supersonic turbulent boundary layer (Elsinga et al. 2010). An example is provided in Fig. 32 that clearly shows arch-shaped (“hairpin like”) coherent structures, “embracing” a low speed region (u is the fluctuating velocity, U_e the free stream velocity and δ the boundary layer thickness).

4.2 Particle Preferential Segregation

It has been shown both numerically as well as experimentally that hairpin vortices appear in “trains” (van Hout 2013; Zhou et al. 1999) having a longitudinal extent of

Fig. 32 Instantaneous vortex distribution detected by the Q -criterion (green) and low-speed zones (blue) in the buffer layer $15 < y^+ < 145$ of a turbulent boundary layer (Jodai et al. 2014)

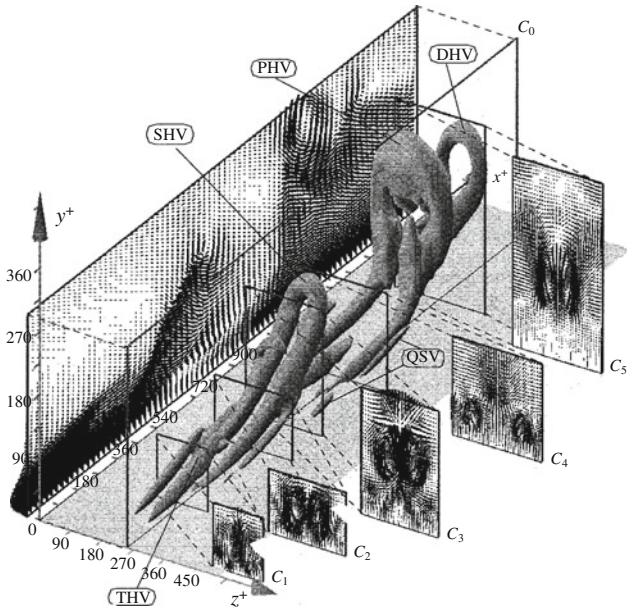
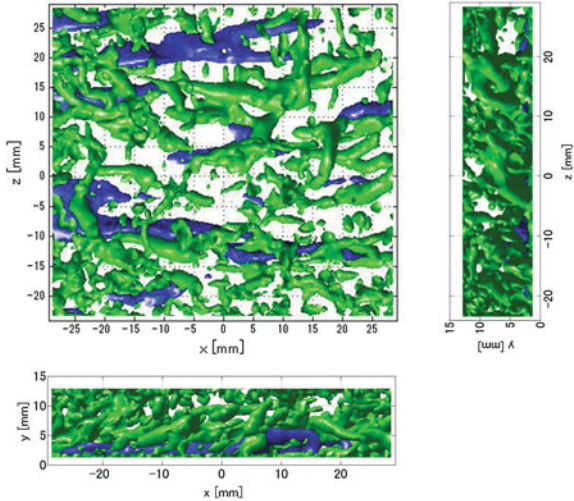
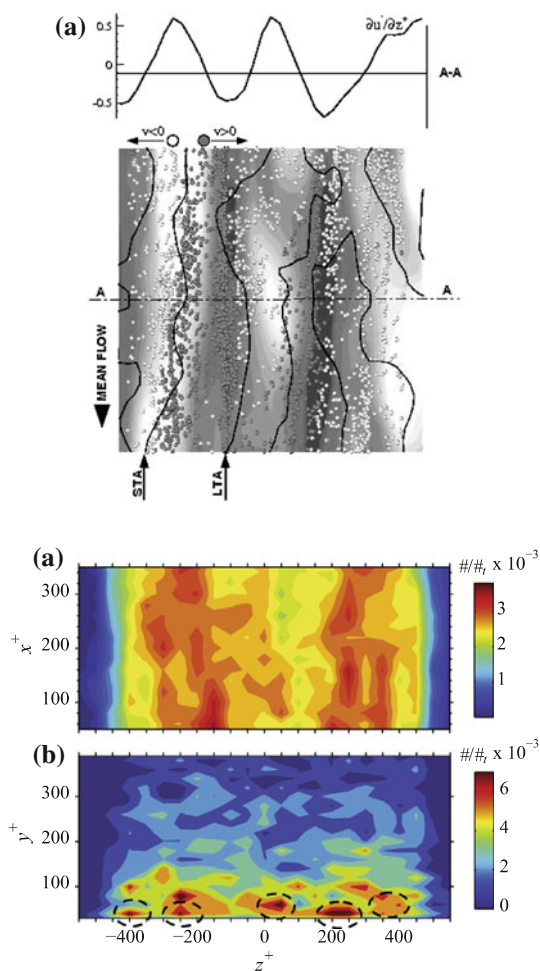


Fig. 33 Sequence of hairpin vortices. (Adrian 2007)

several hundreds of wall units (see Fig. 33). These sequences of coherent structures can lead to segregation of particles in the near wall region leading to longitudinal streaks widely observed in experiments (Fessler et al. 1994; Rabencov and van Hout 2014; 2015; Rouson and Eaton 2001). For example, the holography measurements performed by Rabencov et al. (2014) revealed preferential lanes of near-neutrally

Fig. 34 **a** Top view of particle distribution in the viscous sublayer of a turbulent boundary layer (DNS) showing particle accumulation in longitudinal, low-speed streaks (Soldati and Marchioli 2009); **b** Measured bead number density distribution in turbulent square channel flow, dashed ellipses indicate “preferred lanes” (Rabencov and van Hout 2014)



buoyant, polystyrene beads in a square channel flow similar as those observed in the DNS by Soldati (2005), see Fig. 34.

4.3 Hydrodynamic Resuspension and Saltation

Particle deposition and (re)-suspension are common in environmental and industrial flows such as in wind and water erosion, chemical and nuclear plants as well as pollen and spore dispersal by plants (e.g. Nicholson 1988; Hall 1989; Fessler et al. 1994; Aylor et al. 2003; Nezu and Azuma 2004; Ferrante and Elghobashi 2004;

Soldati and Marchioli 2009). Suspension (initial entrainment) and resuspension, i.e. re-entrainment of prior deposited particles into the bulk of the fluid, are often difficult to distinguish and in the following the term resuspension will be used for both processes. Resuspension has long been regarded as a threshold process governed by the wall shear stress, τ_w , determined from mean flow quantities (Bagnold 1951; Francis 1973; Shields 1936; White 1970). However, it is by now well accepted that particle deposition onto surfaces and resuspension from them is closely related to coherent structures (Robinson 1991) that reside in turbulent boundary layers. Many experiments have shown that particle removal from surfaces is of random nature and is closely related to the existence of strong ejection-sweep cycles (“bursts”) in the near wall region (e.g. Marchioli and Soldati 2002; Soldati 2005). However, the complex interaction between these “bursts” and deposition and resuspension is still poorly understood.

The present view of a turbulent boundary is one in which coherent structures exist that penetrate or even originate in the viscous sublayer (e.g. Zhou et al. 1999; Sheng et al. 2009). Without describing the specific topology of different types of coherent structures, most researchers agree that alternating ejection-sweep cycles are extremely important in momentum, heat and mass transfer from the wall into the bulk turbulent flow. While sweeps, i.e. fast downward moving flow, carry fluid towards the wall, slow upward moving fluid ejections do the opposite. These coherent structures carry particles with them provided the ejection-sweep cycles are sufficiently strong. Sutherland (1967) was one of the first to propose a mechanism that explained the experimentally observed erratic “burst” type resuspension of particles immersed in the viscous sublayer. He hypothesized that coherent turbulent eddies strong enough to penetrate the viscous sublayer were responsible of lifting up particles provided the induced wall-normal fluid velocity exceeded the particle’s gravitational and adhesive forces. Cleaver and Yates (1973) further developed this notion of “burst” controlled resuspension of small particles and suggested a two stage lift up process in which a particle was initially lifted up by a “burst”, followed by another one that carried the particle out of the viscous sublayer into the bulk of the fluid (Fig. 35).

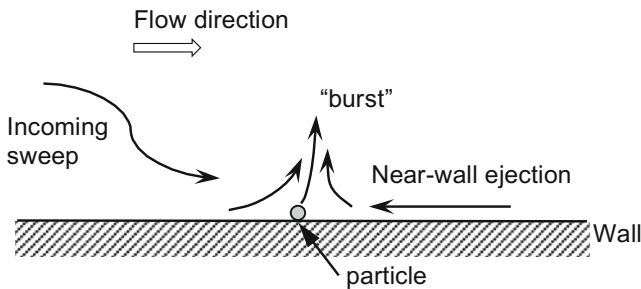


Fig. 35 Schematic representation of a turbulent burst in the wall region

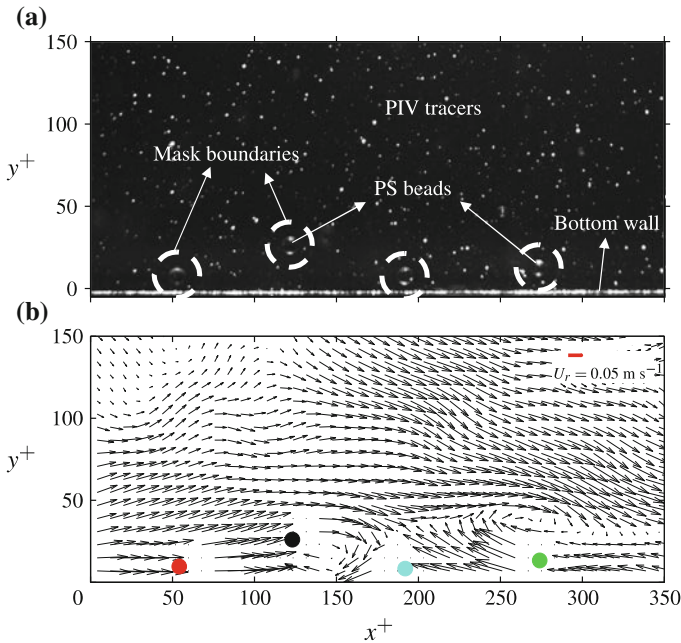


Fig. 36 Example of data processing procedure: **a** part of PIV image including PS beads and masks (*dashed circles*); **b** processed PIV image of fluid velocity fluctuations (Reynolds-decomposed) and superposed beads. Reprinted with permission (van Hout 2013)

Case study on particle resuspension and saltation. Experiments (van Hout 2013) were performed in order to both temporally and spatially track suspended polystyrene (PS) beads and fluid motion in a turbulent boundary layer. Nearly neutrally buoyant PS beads ($\rho_p = 1050 \text{ kg m}^{-3}$, Microbeads AS), with nominal diameter $d = 583 \pm 14.4 \mu\text{m}$ ($d^+ = 10$), were introduced into the flow sufficiently long before the start of the experiment to obtain a well-mixed suspension. The goal of the study by van Hout (2013) was to provide insight into the physical mechanisms that govern particle resuspension and saltation. Time-resolved (high-speed) PIV and PTV measurements were performed in a turbulent water channel flow, temporally and spatially resolving the motion of the fluid and of the dispersed, nearly neutrally buoyant polystyrene beads ($d^+ \approx 10$). The reader is referred to van Hout (2013) for further information regarding the experimental setup and conditions.

Due to the low particle volume fraction, PS beads could be individually tracked over consecutive images. An example of part of a PIV image that includes PS beads is displayed in Fig. 36a. Beads entering the FOV were identified and tracked using a direct cross-correlation procedure (see Sect. 3.1).

The trajectories of the centroid positions of P_1 – P_4 are shown in Fig. 37 at half the actual temporal resolution. All beads lift off the wall but the trajectories of P_1 and P_2 are clearly different and will be discussed in detail. The position where particles P_1

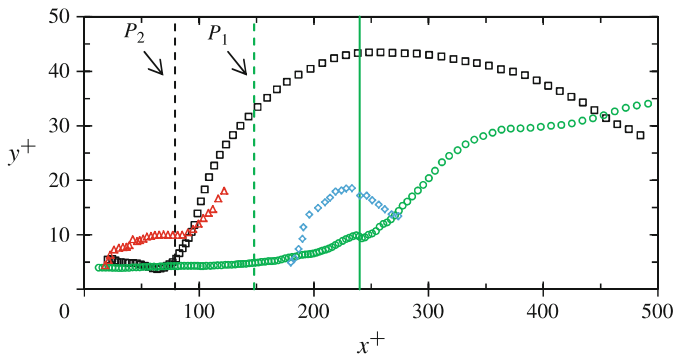


Fig. 37 Bead centroid trajectories. The colours correspond to the beads in Fig. 36: \circ , P_1 (green); \square , P_2 (black); \triangle , P_3 (red); \diamond , P_4 (blue). The dashed lines denote the x^+ position where the bead leaves the surface (estimated from PIV images); the solid line indicates the start of second-stage lift-up of P_1 . Reprinted with permission from van Hout (2013)

and P_2 left the wall was estimated from the original PIV images and is indicated by dashed lines in Fig. 37. At $x^+ = 148$, P_1 slowly lifts off the wall at a shallow angle. Subsequently, it strongly lifts up and around $x^+ = 350$ ($y^+ = 30$), the trajectory flattens but the bead does not settle down. Note that this type of resuspension is similar to the two-stage lift-off proposed by Cleaver and Yates (1973) for particles submerged in the viscous sublayer. We therefore term P_1 's lift-off between $x^+ = 148$ and 235 as first-stage lift-off, and from there on as second-stage lift-off (the start is indicated by the solid line). On the other hand, P_2 displays a very rapid increase in height, taking off at a steep angle ($\sim 35^\circ$) at $x^+ = 79$ and reaching a height of $y^+ = 30$ within $\Delta x^+ = 100$, i.e. twice as fast as P_1 . Bead P_2 reaches a maximum height of $y^+ = 43.5$, after which it slowly descends; its trajectory shape is similar to saltation trajectories observed in several other studies (Ancy et al. 2002; Francis 1973; White and Schulz 1977). Further, note that resuspension of P_4 resembles that of P_2 although a much lower height is attained, while the trajectory of P_3 shows some resemblance to P_1 .

In order to investigate the spatio-temporal interaction of the PS beads with near-wall coherent structures one can visualize them using the out-of-plane vorticity, ω_3 , and the directional swirling strength, Λ_{ci} , in conjunction with the instantaneous $u_1 u_2$ correlations and streamwise velocity fluctuations (see also van Hout 2011). The PIV vector maps were used to calculate the out-of-plane component of the vorticity, $\omega_3 = (\partial U_2 / \partial x_1 - \partial U_1 / \partial x_2)$. Derivatives were calculated using a center-difference scheme. As a means to detect vortex cores, the swirling strength is used, which is a well-accepted parameter to detect vortical structures in turbulent flows. It is based on the imaginary part of the complex eigenvalue of the velocity gradient tensor being larger than zero, $\lambda_{ci} > 0$ (Zhou et al. 1999). In the case of 2D-PIV, not all terms of the local velocity gradient tensor are known and in this case the eigenvalue is determined from an equivalent 2D tensor (Adrian et al. 2000). Here, we follow the work of Wu

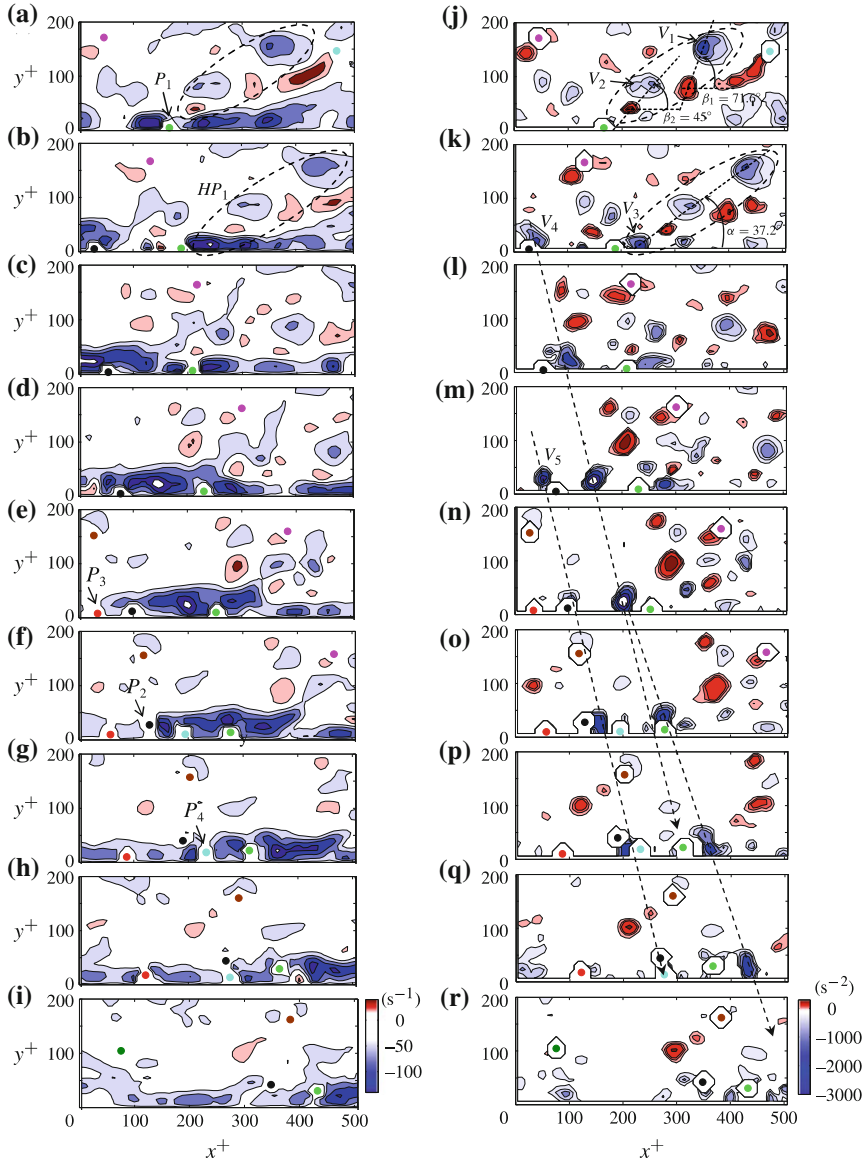


Fig. 38 Sequence ($\Delta t^+ = 4.45$) of **a-i** vorticity, and **j-r** swirling strength. PS beads are superposed. The *dashed ellipses* indicate a hairpin packet. Reprinted with permission (van Hout 2013)

and Christensen (2006) and define a modified swirling strength parameter (from here on termed as the swirling strength) that retains the vortex rotation direction, $\Lambda_{ci} = \lambda_{ci} \omega_3 / |\omega_3|$. Note that the swirling strength is preferred over the vorticity for

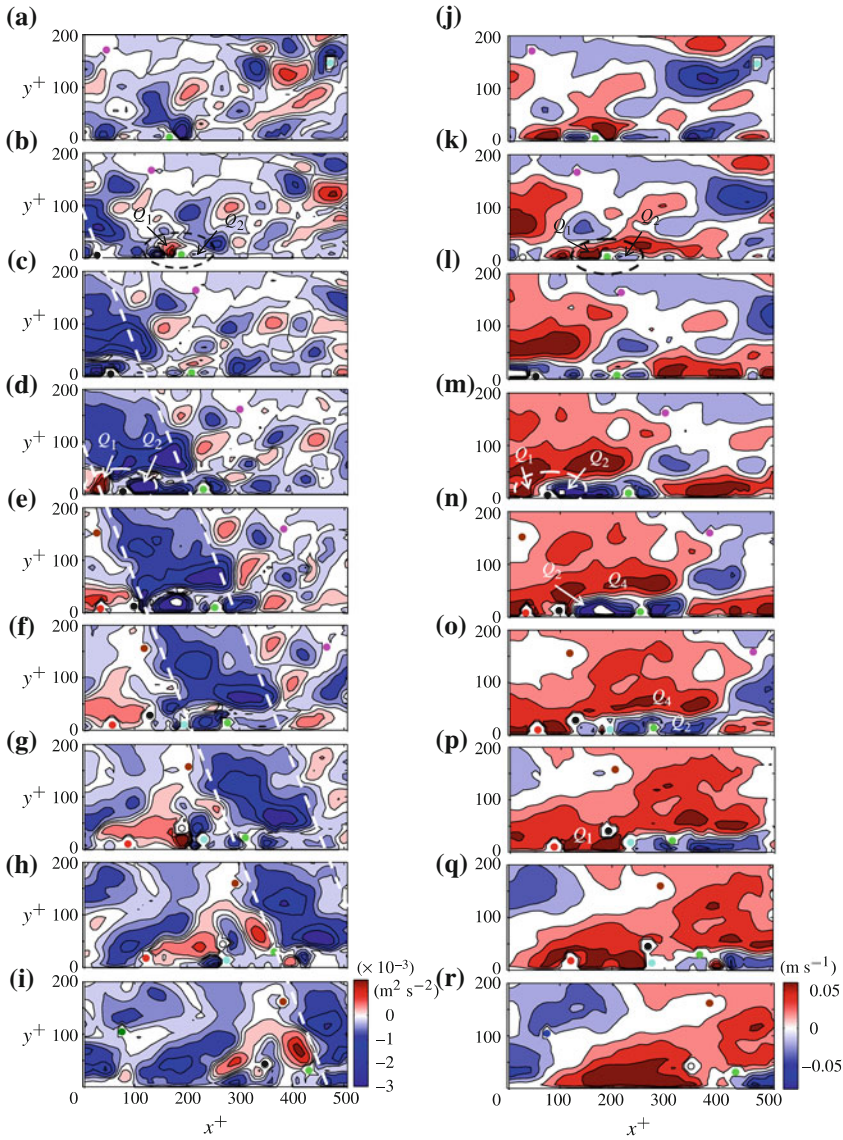


Fig. 39 Sequence ($\Delta t^+ = 4.45$) of **a–i** instantaneous fluctuating velocity correlations, $u_1 u_2$, and **j–r** fluctuating streamwise velocity, u_1 . PS beads are superposed. Reprinted with permission (van Hout 2013)

the detection of vortex cores since it does not reveal areas that have significant vorticity such as shear layers, but lack any local swirling motion.

The spatial distributions of vorticity and swirling strength are shown in Fig. 38 together with the superposed beads. In addition, distributions of instantaneous $u_1 u_2$

correlations and u_1 are shown in Fig. 39. The vorticity and swirling strength maps (Fig. 38a–b and j–k) show a succession of three strong clockwise rotating vortex cores V_1 to V_3 ; V_1 and V_2 form pairs with much smaller magnitude counter-rotating vortices (their centers joined by dotted lines in Fig. 38j), each a 2D spatial signature of an Ω -shaped hairpin (van Hout 2011; Zhou et al. 1999). This train of uplifted structures is known to be the 2D spatial signature of “hairpin” packets (dashed ellipses in Fig. 38a–b, j–k; see also van Hout 2011; Zhou et al. 1999). This “hairpin” packet (HP_1) has a streamwise extent of $\Delta x^+ \approx 250$ and the mean angle with the wall is $\alpha \approx 37.2^\circ$, steeper than values reported by Zhou et al. (1999). The counter-rotating vortex pairs V_1 and V_2 are inclined at angles $\beta_1 = 71.6^\circ$ and $\beta_2 = 45.0^\circ$, respectively, values that compare well with those given by Zhou et al. (1999). The passage of HP_1 coincides with P_1 ’s first stage lift-off between $x^+ = 148$ and 235 (Fig. 38). In addition, two strong clockwise rotating vortex cores, V_4 and V_5 , are located close to the wall in the swirling strength maps of Fig. 38k–q, their position indicated by the dashed arrows. These two vortices are closely associated with a region of high vorticity near to the wall (Fig. 38b–h) and both move faster than P_1 and P_2 . As V_4 passes P_1 around $x^+ = 275$, P_1 strongly accelerates and enters its second stage lift-off (Fig. 37). Similarly, P_2 ’s lift-off coincides with the passage of V_5 (Fig. 38m–o).

The corresponding spatial distributions of instantaneous $u_1 u_2$ correlations (Fig. 39a–i) and u_1 (Fig. 39j–r) provide additional information and by combining them we can identify different quadrant motions (Lu and Willmarth 1973; Willmarth and Lu 1972), i.e. outward interaction ($u_1 > 0, u_2 > 0, Q_1$), ejection ($u_1 < 0, u_2 > 0, Q_2$), inward interaction ($u_1 < 0, u_2 < 0, Q_3$) and sweep ($u_1 > 0, u_2 < 0, Q_4$). The $u_1 u_2$ correlation maps show a strong spatially coherent region of negative $u_1 u_2$ (between dashed lines in Fig. 39b–i) followed by positive $u_1 u_2$ closer to the wall (Fig. 39d–i). The u_1 maps indicate that both these regions are mainly associated with $u_1 > 0$, besides a thin slice near the wall in which especially P_1 is submerged during lift off. The different quadrant motions associated with the resuspension of P_1 to P_4 are illustrated in Fig. 39. When P_2 leaves the wall at $x^+ = 79$, it is located at the interface between an upstream outward interaction and a downstream ejection close to the wall (see dashed ellipses in Fig. 39d and m), very similar to the resuspension mechanism sketched by Cleaver and Yates (1973) and the sequence of events measured by Braaten et al. (1990). This flow pattern is induced by the passage of V_4 and V_5 (Figs. 38 and 39l–n). Note that the same sequence of events though less pronounced, occurs as V_3 passes P_1 (Fig. 39b and k).

This case study provided a wealth of information on the sequence of events that lead to bead resuspension and saltation, in particular related to coherent structures. However, this type of data can also be used to estimate the forces acting on particles in suspensions (Kurose and Komori 1999; Lee and Balachandar 2010; Nalpanis et al. 1993; Phillips 1980; Takemura and Magnaudet 2003; White and Schulz 1977; Wiberg and Smith 1985; Zeng et al. 2005). Wiberg and Smith (1985) developed a simple model based on Bernoulli principles for the prediction of the lift and drag force while Krishnan and Leighton (1995) showed that the lift force in the limit of Stokes flow is a superposition of six contributions, i.e. ambient shear, translational and rotational motions of the particle as well as their binary couplings. The latter

result was further expanded by Zeng et al. (2009) and Lee and Balachandar (2010) to small but finite Reynolds numbers. For further information on the estimation of the instantaneous lift force acting on the particle, the reader is referred to van Hout (2013).

5 State-of-the-Art Measurements as Outlook for Future Developments

In this chapter, two state-of-the-art measurements are introduced, both using tomographic PIV measurements.

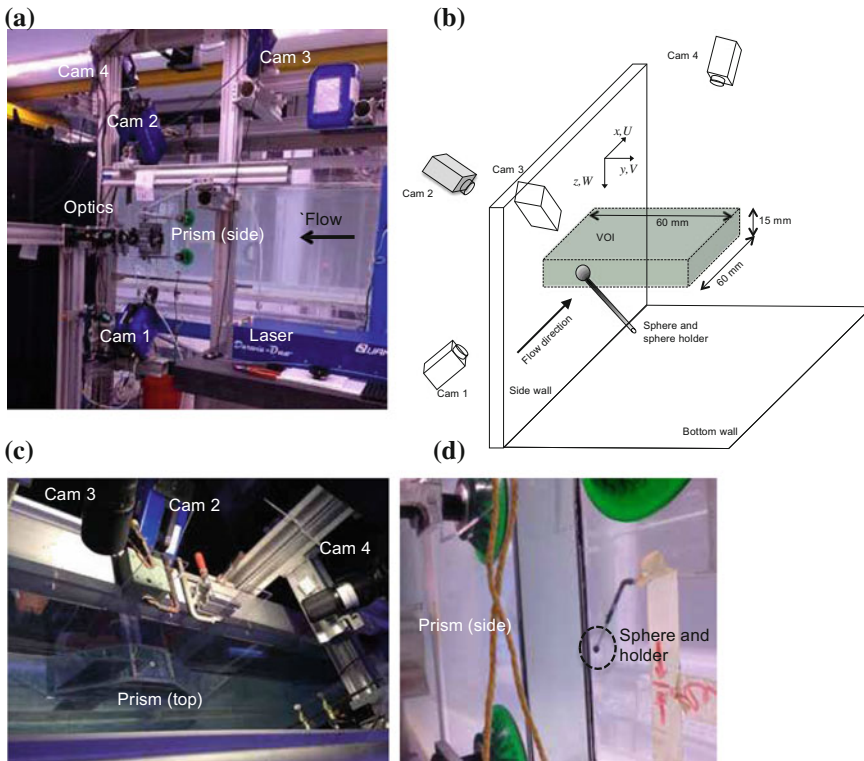


Fig. 40 Water tunnel experimental setup, **a** Side view of 4 camera tomo-PIV, **b** Schematic layout (not to scale), **c** top view and **d** Close-up of stationary sphere and holder

5.1 Case Study of the Interaction of a Stationary Sphere with a Turbulent Boundary Layer

In the following, a case study of a stationary held sphere immersed at different heights into a flat plate turbulent boundary layer is discussed. Measurements were done using tomographic-PIV. This study can be extended in future studies to freely moving spheres in a turbulent boundary layer.

Experimental setup. Experiments were performed in the water tunnel of the laboratory for Aero- and Hydrodynamics at Delft University of Technology. The tunnel had a cross section of $600 \times 600 \text{ mm}^2$. Due to setup constraints, measurements were performed in the boundary layer that was formed on the vertical channel, side-wall made of transparent plexiglass. In order to force transition to turbulence, a zigzag strip (Elsinga and Westerweel 2010) was placed 50 cm downstream of the test section's inlet. The tomo-PIV setup (see Fig. 40) comprised four high-speed Imager-Pro HS cameras (2016×2016 pixels), a high-speed laser (Nd:YLF, Darwin Duo 80M, Quantronix), optics/prisms and data acquisition/processing software (LaVision, DaVis8.2).

Time resolved tomo-PIV measurements were performed 3.5 m downstream of the trip at three different bulk flow velocities, i.e. 0.085, 0.17 and 0.34 m/s, corresponding to bulk Reynolds numbers, $\text{Re}_b = U_b H / \nu = 51 \times 10^3$, 102×10^3 and 204×10^3 , where $H = 0.6 \text{ m}$ is the channel depth, U_b the bulk flow velocity and ν the kinematic

Table 1 Overview of experimental conditions of tomo-PIV of stationary held sphere

Data set	U_b [m/s]	Re_b $\times 10^3$	f_a [Hz]	h [mm]	h^+	u_τ [m/s]	ν/u_τ [mm]	ν/u_τ^2 [ms]	D^+
TS5_1,2	0.085	51	150	-	-	0.00425	0.235	55	25.5
TSS5_2				5.4	23.0				
TSS5_1				10.3	43.8				
TSS5_3				37.5	159.4				
TS10_1,2	0.17	102	250	-	-	0.0082	0.118	14	51.0
TSS10_2				5.4	45.9				
TSS10_1				10.3	87.6				
TSS10_3				37.5	318.8				
TS20_1,2	0.34	204	475	-	-	0.17	0.059	3.5	102.0
TSS20_2				5.4	91.8				
TSS20_1				10.3	175.1				
TSS20_3				37.5	637.5				

Vector spacing = 0.32 mm (75 % overlap), Voxel size = 1.28 mm or $10.5y^+$ (for $U_b = 0.17 \text{ m/s}$)

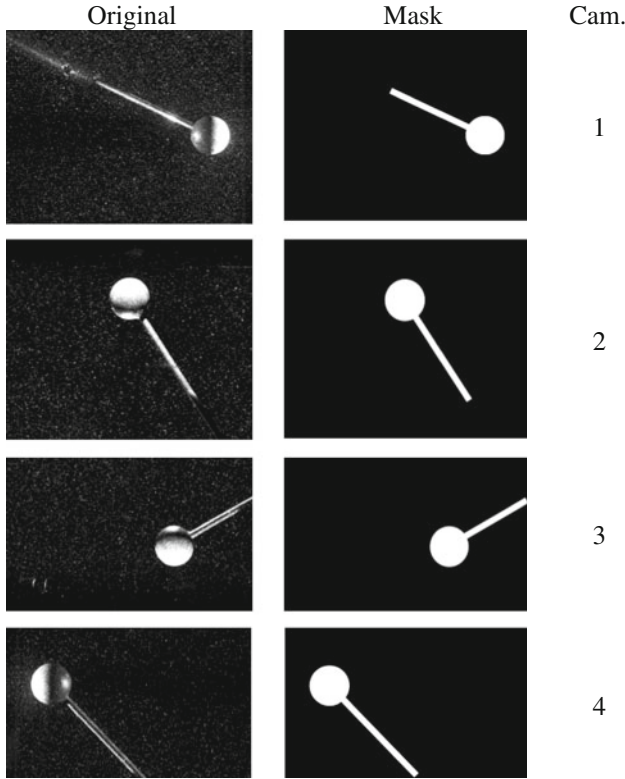


Fig. 41 The stationary sphere as seen by the different cameras. *Left column* original PIV images, *right column* masks

viscosity. The volume of interest consisted of a horizontal slab with dimensions of $60 \times 15 \times 60$ mm ($L \times D \times W$). In order to make sure that the light intensity was sufficient and cameras benefitted from forward light scattering, a mirror was used to reflect the light back. Additionally, this helped in diminishing shadow effects of the stationary held sphere. The volume of interest (VOI) was located in the middle of the channel height, 30 cm above the bottom wall. As flow tracers, near-neutrally buoyant hollow glass spheres (Sphericell, Potter's industries) were used. At each flow condition a sphere having a diameter of $D = 6.0$ mm, held in place by a cylindrical rod ($d = 1.0$ mm), was positioned at three different distances from the wall, i.e. $h = 7.4$, 12.3 and 39.5 mm, where h denotes the distance between the sphere's center and the wall position. An overview of the experimental conditions is shown in Table 1. At each flow condition, two data sets were acquired (acquisition frequency, f_a) without sphere and for each sphere position, one data set was acquired. The friction velocity, u_τ , was determined by a Clauser fit and the superscript “+” denotes inner wall scaling.

Different cropped views as seen by the four cameras of original PIV images are depicted in Fig. 41a. Based on these images, for each of the views, a mask was constructed using Photoshop (Fig. 41b). These masks were then re-imported into

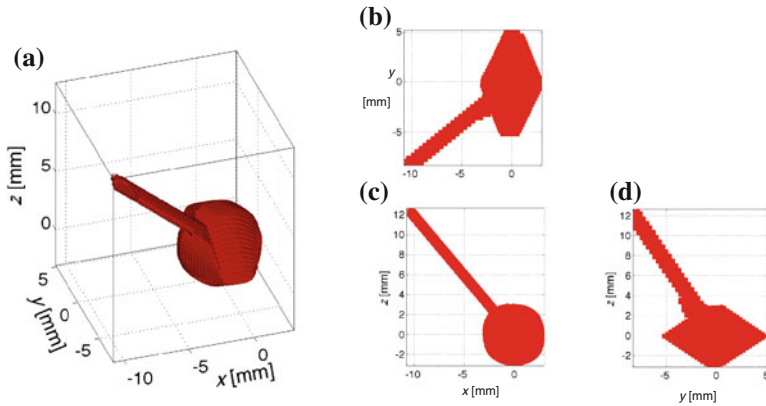


Fig. 42 Reconstructed visual hull in **a** 3D, **b** x - y plane, **c** x - z plane and in **d** y - z plane

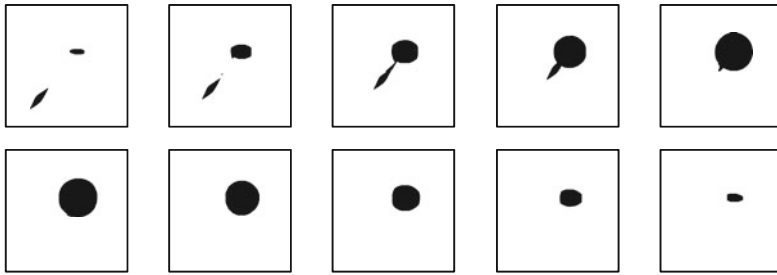


Fig. 43 Binary images of x - y planes of the visual hull at different z -positions ($\Delta z = 30$ voxels, from *left to right*), used to mask the reconstructed particle volumes plane by plane (30 voxels between planes, actual PIV resolution was 10 voxels between planes, 75 % overlap, window size 40 voxels)

DaVis 8.2 software (LaVision) and were reconstructed in the same way as the particles in the VOI using the “fast-MART” algorithm (Adhikari and Longmire 2012).

The resulting visual hull is depicted in Fig. 42a at the same resolution as the vector maps (10 voxels in depth). Projections of the visual hull in the different planes are shown in Fig. 42b–d. Clearly, the visual hull of the sphere looks like a double cone and only the projection in the x - z plane looks like a circle. Note that the exact shape of the visual hull depends on the camera setup. In case more cameras from different viewing angles would be used, the reconstructed visual hull would be more similar to the actual sphere.

The visual hull is used as a mask on the reconstructed particle volume. After particle volume reconstruction, each x - y plane at different depth (z) positions is multiplied by the mask. Examples of the mask images are shown in Fig. 43. Note that it is essential to mask the reconstructed particle volume since at the position of the sphere, ghost particles appear that affect the cross-correlation algorithm and lead to bad vectors in the neighborhood of the sphere.

The masked particle volumes were then processed using direct correlation of 3D particle volumes (DaVis 8.2, LaVision software) at an interrogation volume size of 40 voxels with 75 % overlap. The data acquired at $U_b = 0.17$ m/s (see Table 1) was processed in multiple steps reducing the interrogation volume size from 96 to 40 voxels in the last step. In between the steps, the obtained vector maps were checked for outliers and smoothed by a $3 \times 3 \times 3$ Gaussian median filter. The obtained vector maps were exported into Matlab where they were subsequently temporally and spatially smoothed using 2nd order polynomial regression over 7 points (Elsinga and Westerweel 2010). The size of the regression interval was of the order of the viscous time scale, $\nu/u_\tau^2 \approx 14$ ms, and the smallest size of the near wall structures (~ 15 inner wall coordinates) and is not expected to remove any relevant information on the near-wall turbulent flow structures. Snapshots of the turbulent flow structures visualized by the Q -criterion (Hunt et al. 1988), are shown in Fig. 44 without and in Figs. 45 and 46 with the stationary sphere positioned closest and furthest from the wall.

Figure 44 clearly indicates the existence of elongated, streamwise vortices stretched along the wall as well as several uplifted structures. Pieces of a span-wise vortical “tube” are seen further away from the wall spanning the width of the measurement volume. When the sphere is inserted furthest from the wall (Fig. 46), the near wall structures can be clearly discerned from those generated by the sphere. However, sphere wake and inner-wall boundary layer may interact and it is of interest to study the effect of the external perturbation on the inner-wall turbulent boundary layer characteristics. When the sphere is closest to the wall (Fig. 45), vortical structures amalgamate.

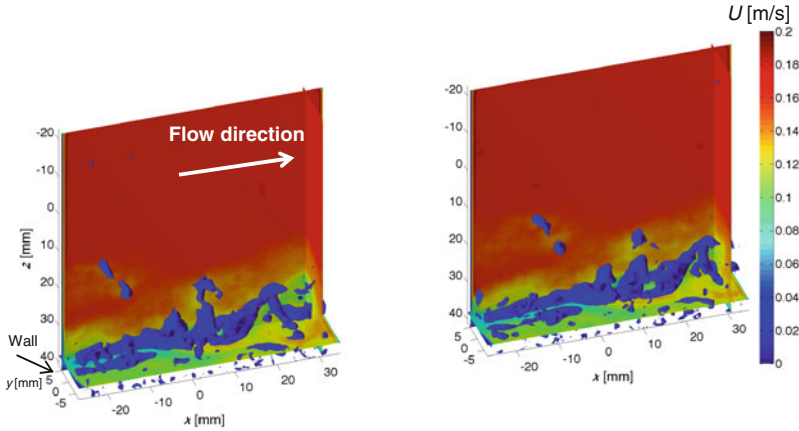


Fig. 44 Examples of snapshots ($\Delta t = 40$ ms) of the mean streamwise flow velocity (contour plots) and turbulence coherent structures (in blue) as visualized by the Q -criterion

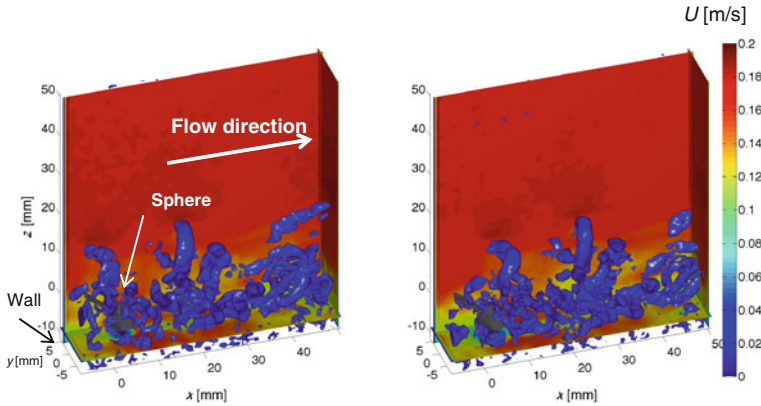


Fig. 45 Examples of snapshots ($\Delta t = 40$ ms) of the mean streamwise flow velocity (contour plots) and turbulence coherent structures (in blue) as visualized by the Q -criterion. Sphere positioned closest to the wall

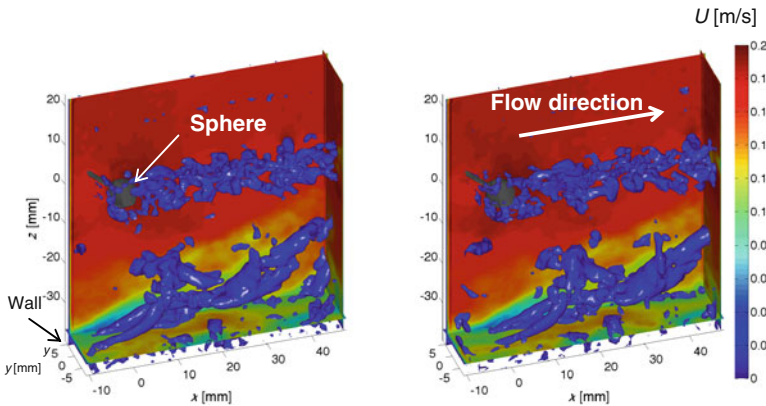


Fig. 46 Examples of snapshots ($\Delta t = 40$ ms) of the mean streamwise flow velocity (contour plots) and turbulence coherent structures (in blue) as visualized by the Q -criterion. Sphere positioned farthest from the wall

5.2 Case Study of “Large” Refractive Index Matched Spheres Freely Moving in a Turbulent Boundary Layer

In this study, refractive index matched, hydrogel beads ($D = 6\text{--}7$ mm) doped with small tracer particles were released from the bottom wall into a fully developed turbulent boundary layer. At about 20 cm downstream of the release point, time-resolved tomo-PIV measurements were performed in order to measure the interaction between a freely moving sphere and the turbulent boundary layer. The aim is to measure both the flow field surrounding the bead as well as rotation/translation of the hydrogel bead.

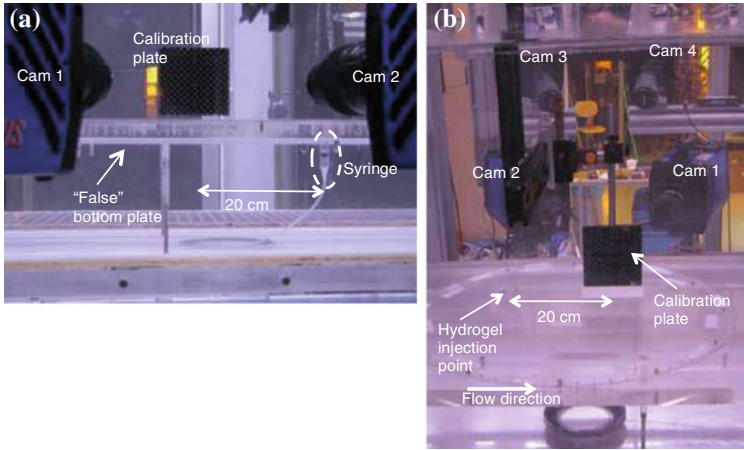


Fig. 47 Pictures of the setup of the syringe and measurement position. View **a** from camera perspective and **b** opposite of cameras

Experimental setup. Experiments were performed in the water tunnel of the laboratory for Aero and Hydrodynamics at Delft University of Technology. The tunnel had a cross section of $600 \times 600 \text{ mm}^2$. However, a false bottom wall was put on stands and laid on top of the actual bottom thus creating an open channel with a cross section of $600 \times 420 \text{ mm}^2$ (width \times height). Hydrogel spheres ($6 < D < 7 \text{ mm}$) were introduced from the bottom through slow manual injection by a syringe (5 ml syringe BD-plastipak, internal diameter of 11 mm). The syringe was flush mounted with the top of the bottom plate and could be removed from the top in order to refill it with hydrogel spheres (see Fig. 47). The distance from the center of the syringe opening to the center of the measurement volume was 20 cm.

Besides the syringe, a much larger thin cover plate was also mounted flush with the bottom plate. At the measurement position between the bottom and cover plate

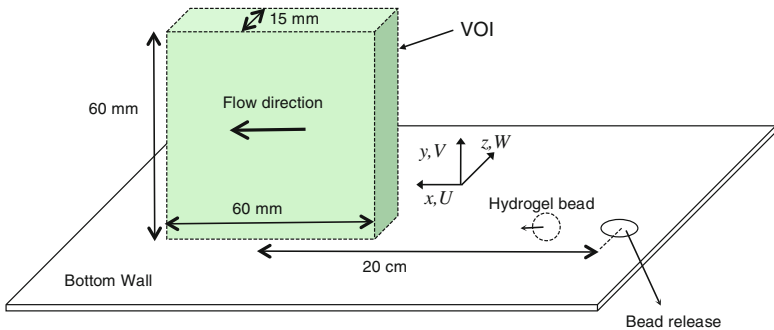


Fig. 48 Schematic layout of hydrogel injection and VOI (not to scale)

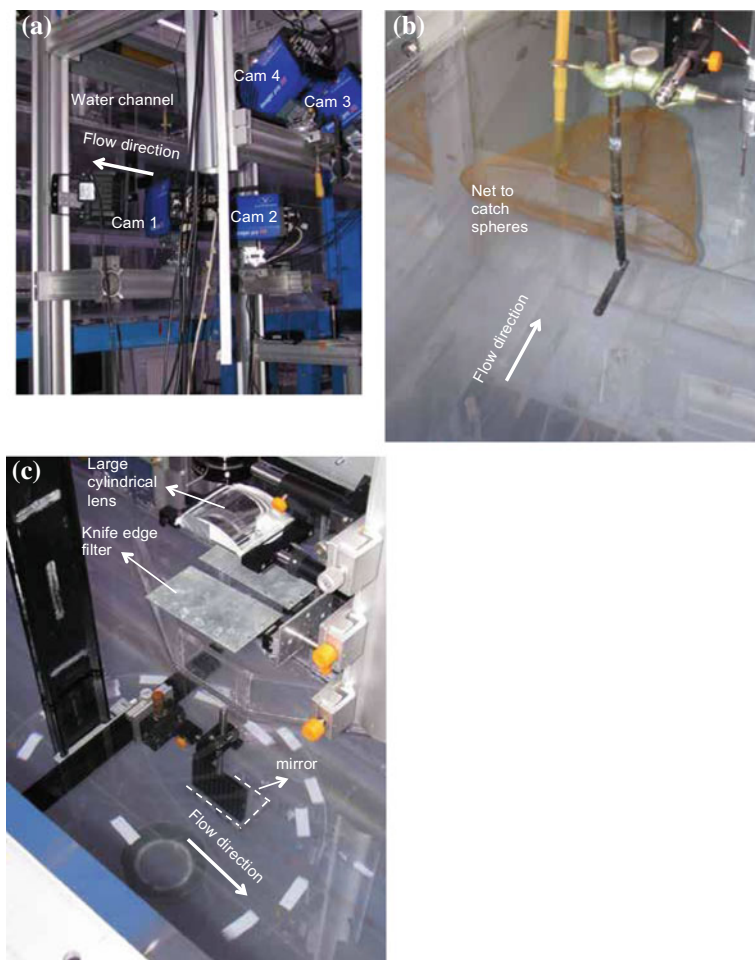


Fig. 49 Pictures of the hydrogel experimental setup. **a** Camera positions looking through the channel's side wall, **b** Optics setup, *top view*, **c** view of the channel exit

a reflecting mirror was placed in order to double the light intensity in the volume of interest. The sphere injection was located 20 cm from the side wall closest to the cameras. The tomographic PIV setup consisted of 4 LaVision Imager Pro HS 4M (Dimax PCO) cameras (2016×2016 pixels, 12 bit), Scheimpflug adapters, optics and a high speed laser (Darwin-Duo 527-80-M, Quantel), 50 mJ/pulse, max 10 kHz. Cameras were positioned on one side of the channel at angles of around 30° without using any prisms to reduce refraction. The latter effectively reduced the cameras' solid angle.

The two bottom cameras (1 and 2) were placed horizontally and were equipped with 105 mm Nikor lenses ($f_{\#} = 16$) while the two upper cameras (3 and 4) were

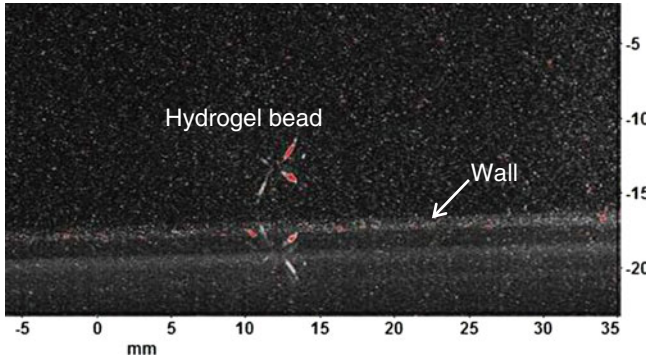


Fig. 50 Raw data obtained from tomo-PIV measurements of hydrogel bead near the *bottom* wall

looking down and were equipped with 200 mm Nikor lenses ($f_{\#} = 22$). The laser volume was created by a knife-edge filter and a large cylindrical lens used to collimate the volume at the edges. It entered the channel from the top aligned with the streamwise direction and the measurement volume dimensions were $60 \times 15 \times 60 \text{ mm}^3$ ($L \times W \times H$). Measurements were performed at three different bulk flow velocities (based on the free cross-section above and below the false bottom plate), $U_b = 0.11, 0.21$ and 0.43 m/s corresponding to bulk Reynolds numbers, $Re_b = U_b H / \nu = 44,184, 88,746$ and $179,508$, where $H = 0.42 \text{ m}$ is the channel depth.

The volume of interest consisted of a vertical slab with dimensions of $60 \times 15 \times 60 \text{ mm}$ ($L \times D \times W$, Fig. 48). In order to make sure that the light intensity was sufficient and cameras benefitted from forward scattering a mirror was used to reflect the light back (Fig. 49). As flow tracers, near-neutrally buoyant hollow glass spheres (Sphericell, Potter's industries) were used.

At each flow condition, two data sets were acquired to characterize the flow without injection and several data sets were acquired while injecting hydrogels. Before injections the hydrogel spheres were injected with sphericell flow tracers (Klein et al. 2013). The injection pattern was a six “spoke” pattern as shown in Fig. 50. The injection was done by placing the sphere on a stand placed on a turntable. Subsequently, a thin injection needle (BD microlance) was dipped into the tracers and injected into and retracted from the sphere.

Note that in this case, a visual hull does not need to be constructed. The whole particle volume can be reconstructed without a-priori masking. The idea is then that the “spokes” can be found as line elements in the reconstructed 3D particle volume by applying a 3D Hough transform.

References

- Adhikari, D., & Longmire, E. K. (2012). Visual hull method for tomographic PIV measurement of flow around moving objects. *Experiments in Fluids*, 53, 943–964. <http://doi.org/10.1007/s00348-012-1338-9>.
- Adrian, R. J. (2007). Hairpin vortex organization in wall turbulence. *Physics of Fluids*, 19, 041301. <http://doi.org/10.1063/1.2717527>.
- Adrian, R. J., Christensen, K. T., & Liu, Z.-C. (2000). Analysis and interpretation of instantaneous turbulent velocity fields. *Experiments in Fluids*, 29, 275–290. <http://doi.org/10.1007/s003489900087>.
- Ancey, C., Bigillon, F., Frey, P., Lanier, J., & Ducret, R. (2002). Saltating motion of a bead in a rapid water stream. *Physical Review E—Statistical, Nonlinear, and Soft Matter Physics*, 66, 1–16. <http://doi.org/10.1103/PhysRevE.66.036306>.
- Aylor, D. E., Schultes, N. P., & Shields, E. J. (2003). An aerobiological framework for assessing cross-pollination in maize. *Agricultural and Forest Meteorology*, 119, 111–129.
- Bagnold, R. A. (1951). The movement of a cohesionless granular bed by fluid flow over it. *British Journal of Applied Physics*, 2, 29–34. <http://doi.org/10.1088/0508-3443/2/2/301>.
- Bellani, G., Byron, M. L., Collignon, A. G., Meyer, C. R., & Variano, E. (2012). Shape effects on turbulent modulation by large neutrally buoyant particles. *Journal of Fluid Mechanics*, 712, 41–60.
- Bianchi, D. E., Schwemmin, D. J., & Wagner, W. H., Jr. (1959). Pollen release in the common ragweed (*Ambrosia artemisiifolia*). *Botanical Gazette*, 120, 235–243.
- Born, M., & Wolf, E. (1999). *Principles of optics: Electromagnetic theory of propagation, interference and diffraction of light*. Cambridge: Cambridge University Press.
- Braaten, D. A., Paw U, K. T., & Shaw, R. H. (1990). Particle resuspension in a turbulent boundary layer—observed and modeled. *Journal of Aerosol Science*, 21, 613–628. [http://doi.org/10.1016/0021-8502\(90\)90117-G](http://doi.org/10.1016/0021-8502(90)90117-G).
- Byron, M. L., & Variano, E. A. (2013). Refractive-index-matched hydrogel materials for measuring flow–structure interactions. *Experiments in Fluids*, 54, 1456. <http://doi.org/10.1007/s00348-013-1456-z>.
- Choi, Y.-S., & Lee, S.-J. (2009). Three-dimensional volumetric measurement of red blood cell motion using digital holographic microscopy. *Applied Optics*, 48, 2983–2990. <http://doi.org/10.1364/AO.48.002983>.
- Choi, Y.-S., & Lee, S.-J. (2011). High-accuracy three-dimensional position measurement of tens of micrometers size transparent microspheres using digital in-line holographic microscopy. *Optics Letters*, 36, 4167. <http://doi.org/10.1364/OL.36.004167>.
- Chong, M. S., Perry, A. E., & Cantwell, B. J. (1990). A general classification of three-dimensional flow fields. *Physics of Fluids A: Fluid Dynamics*, 2, 765–777. <http://doi.org/10.1063/1.857730>.
- Cleaver, J., & Yates, B. (1973). Mechanism of detachment of colloidal particles from a flat substrate in a turbulent flow. *Journal of Colloid and Interface Science*, 44, 464–474. [http://doi.org/10.1016/0021-9797\(73\)90323-8](http://doi.org/10.1016/0021-9797(73)90323-8).
- Collier, R. (2013). *Optical holography*. Elsevier.
- Elsinga, G. E., & Westerweel, J. (2010). Tomographic-PIV measurement of the flow around a zigzag boundary layer trip. In *15th International Symposium on Applications of Laser Techniques to Fluid Mechanics*. Lisbon, Portugal, 05–08 July (pp. 5–8).
- Elsinga, G. E., Adrian, R. J., van Oudheusden, B. W., & Scarano, F. (2010). Three-dimensional vortex organization in a high-Reynolds-number supersonic turbulent boundary layer. *Journal of Fluid Mechanics*, 644, 35–60. <http://doi.org/10.1017/S0022112009992047>.
- Elsinga, G. E., Scarano, F., Wieneke, B., & Van Oudheusden, B. W. (2006). Tomographic particle image velocimetry. *Experiments in Fluids*, 41, 933–947. <http://doi.org/10.1007/s00348-006-0212-z>.

- Elsinga, G. E., Westerweel, J., Scarano, F., & Novara, M. (2011). On the velocity of ghost particles and the bias errors in Tomographic-PIV. *Experiments in Fluids*, 50, 825–838. <http://doi.org/10.1007/s00348-010-0930-0>.
- Ferrante, A., & Elghobashi, S. (2004). On the physical mechanisms of drag reduction in a spatially developing turbulent boundary layer laden with microbubbles. *Journal of Fluid Mechanics*, 503, 345–355.
- Fessler, J., Kulick, J., & Eaton, J. (1994). Preferential concentration of heavy particles in a turbulent channel flow. *Physics of Fluids*, 6, 3742–3749. <http://doi.org/10.1063/1.868445>.
- Fournier, C., Ducottet, C., & Fournel, T. (2004). Digital in-line holography: influence of the reconstruction function on the axial profile of a reconstructed particle image. *Measurement Science and Technology*, 15, 686–693. <http://doi.org/10.1088/0957-0233/15/4/010>.
- Francis, J. R. D. (1973). Experiments on the motion of solitary grains along the bed of a water-stream. *Proceedings of the Royal Society A: Mathematical, Physical and Engineering Sciences*, 332, 443–471. <http://doi.org/10.1098/rspa.1973.0037>.
- Gabor, D. (1948). A new microscopic principle. *Nature*, 161, 777–778. <http://doi.org/10.1038/161777a0>.
- Gonzalez, R. C., & Woods, R. E. (2002). *Digital image processing*. Prentice Hall, Inc.
- Goodman, J. W. (2005). *Introduction to Fourier optics*. Roberts and Company Publishers.
- Hall, D. (1989). The time dependence of particle resuspension. *Journal of Aerosol Science*, 20, 907–910.
- Hariharan, P. (1996). *Optical Holography: Principles, techniques and applications*. Cambridge University Press.
- Hunt, J. C. R., Wray, A. A., & Moin, P. (1988). Eddies, streams, and convergence zones in turbulent flows. In *Center for Turbulence Research, Proceedings of the Summer Program* (pp. 193–208).
- Hwang, W., & Eaton, J. K. (2004). Creating homogeneous and isotropic turbulence without a mean flow. *Experiments in Fluids*, 36, 444–454. <http://doi.org/10.1007/s00348-003-0742-6>.
- Jain, A. K. (1989). *Fundamentals of digital image processing*. Prentice Hall.
- Jeong, J., & Hussain, F. (1995). On the identification of a vortex. *Journal of Fluid Mechanics*, 285, 69. <http://doi.org/10.1017/S0022112095000462>.
- Jodai, Y., Westerweel, J., & Elsinga, G. E. (2014). Time-resolved Tomographic-PIV measurement in the near-wall region of a turbulent boundary layer. In *17th International Symposium on Applications of Laser Techniques to Fluid Mechanics*, Lisbon, Portugal, 07–10 July.
- Kabsch, W. (1976). A solution for the best rotation to relate two sets of vectors. *Acta Crystallographica Section A*, 32, 922–923. <http://doi.org/10.1107/S0567739476001873>.
- Katz, J., & Sheng, J. (2010). Applications of holography in fluid mechanics and particle dynamics. *Annual Review of Fluid Mechanics*, 42, 531–555. <http://doi.org/10.1146/annurev-fluid-121108-145508>.
- Klein, S., Gibert, M., Bérut, A., & Bodenschatz, E. (2013). Simultaneous 3D measurement of the translation and rotation of finite-size particles and the flow field in a fully developed turbulent water flow. *Measurement Science and Technology*, 24, 024006. <http://doi.org/10.1088/0957-0233/24/2/024006>.
- Koek, W. (2006). *Holographic particle image velocimetry using bacteriorhodopsin*. TU-Delft.
- Kolář, V. (2007). Vortex identification: New requirements and limitations. *International Journal of Heat and Fluid Flow*, 28, 638–652. <http://doi.org/10.1016/j.ijheatfluidflow.2007.03.004>.
- Krishnan, G., & Leighton, D. (1995). Inertial lift on a moving sphere in contact with a plane wall in a shear flow. *Physics of Fluids*, 7, 2538. <http://doi.org/10.1063/1.869264>.
- Kurose, R., & Komori, S. (1999). Drag and lift forces on a rotating sphere in a linear shear flow. *Journal of Fluid Mechanics*, 384, 183–206. <http://doi.org/10.1017/S0022112099004164>.
- Langehanenberg, P., Kemper, B., Dirksen, D., & von Bally, G. (2008). Autofocusing in digital holographic phase contrast microscopy on pure phase objects for live cell imaging. *Applied Optics*, 47, D176–D182. <http://doi.org/10.1364/AO.47.00D176>.
- Lee, H., & Balachandar, S. (2010). Drag and lift forces on a spherical particle moving on a wall in a shear flow at finite Re. *Journal of Fluid Mechanics*, 657, 89–125. <http://doi.org/10.1017/S0022112010001382>.

- Leith, E. N., & Upatnieks, J. (1962). Reconstructed wavefronts and communication theory. *Journal of the Optical Society of America*, 52(10), 1123. <http://doi.org/10.1364/JOSA.52.001123>.
- Liu, X., & Katz, J. (2006). Instantaneous pressure and material acceleration measurements using a four-exposure PIV system. *Experiments in Fluids*, 41(2), 227–240. <http://doi.org/10.1007/s00348-006-0152-7>.
- Lu, S. S., & Willmarth, W. W. (1973). Measurements of the structure of the Reynolds stress in a turbulent boundary layer. *Journal of Fluid Mechanics*, 60, 481. <http://doi.org/10.1017/S0022112073000315>.
- Maas, H. G., Gruen, A., & Papantoniou, D. (1993). Particle tracking velocimetry in 3-dimensional flows. Particle tracking velocimetry in three-dimensional flows. Part 1. Photogrammetric determination of particle coordinates. *Experiments in Fluids*, 15(2), 133–146. <http://doi.org/10.1007/BF00190953>.
- Marchioli, C., & Soldati, A. (2002). Mechanisms for particle transfer and segregation in a turbulent boundary layer. *Journal of Fluid Mechanics*, 468, 283–315.
- Milgram, J. H., & Li, W. (2002). Computational reconstruction of images from holograms. *Applied Optics*, 41(5), 853–864. <http://doi.org/10.1364/AO.41.000853>.
- Murata, S., & Yasuda, N. (2000). Potential of digital holography in particle measurement. *Optics and Laser Technology*, 32, 567–574. [http://doi.org/10.1016/S0030-3992\(00\)00088-8](http://doi.org/10.1016/S0030-3992(00)00088-8).
- Nalpanis, P., Hunt, J. C. R., & Barrett, C. F. (1993). Saltating particles over flat beds. *Journal of Fluid Mechanics*, 251:661. <http://doi.org/10.1017/S0022112093003568>.
- Nezu, I., & Azuma, R. (2004). Turbulence characteristics and interaction between particles and fluid in particle-laden open channel flows. *Journal of Hydraulics Engineering*, 988–1001.
- Nicholson, K. W. (1988). A review of particle resuspension. *Atmospheric Environment*, 22, 2639–2651.
- Olson, J. A. (2001). The motion of fibres in turbulent flow, stochastic simulation of isotropic homogeneous turbulence. *International Journal of Multiphase Flow*, 27, 2083–2103. [http://doi.org/10.1016/S0301-9322\(01\)00050-7](http://doi.org/10.1016/S0301-9322(01)00050-7).
- Pan, G., & Meng, H. (2003). Digital holography of particle fields: Reconstruction by use of complex amplitude. *Applied Optics*, 42, 827–833. <http://doi.org/10.1364/AO.42.000827>.
- Phillips, M. (1980). A force balance model for particle entrainment into a fluid stream. *Journal of Physics D: Applied Physics*, 13, 221–233. <http://doi.org/10.1088/0022-3727/13/2/019>.
- Rabencov, B., & van Hout, R. (2015). Voronoi analysis of beads suspended in a turbulent square channel flow. *International Journal of Multiphase Flow*, 68, 10–13. <http://doi.org/10.1016/j.ijmultiphaseflow.2014.09.007>.
- Rabencov, B., Arca, J., & van Hout, R. (2014). Measurement of polystyrene beads suspended in a turbulent square channel flow: Spatial distributions of velocity and number density. *International Journal of Multiphase Flow*, 62, 110–122. <http://doi.org/10.1016/j.ijmultiphaseflow.2014.02.004>.
- Raffel, M., Willert, C. E., Wereley, S. T., & Kompenhans, J. (2007). *Particle image velocimetry*. Berlin, Heidelberg: Springer.
- Robinson, K. (1991). Coherent motions in the turbulent boundary layer. *Annual Review of Fluid Mechanics*, 23, 601–639.
- Rouson, D. W. I., & Eaton, J. K. (2001). On the preferential concentration of solid particles in turbulent channel flow. *Journal of Fluid Mechanics*, 428, 149–169. <http://doi.org/10.1017/S0022112000002627>.
- Sabban, L., Jacobson, N.-L., & van Hout, R. (2012). Measurement of pollen clump release and breakup in the vicinity of ragweed (*A. confertiflora*) staminate flowers. *Ecosphere*, 3, 1–24. <http://doi.org/10.1890/ES12-00054.1>.
- Sabban, L., & van Hout, R. (2011). Measurements of pollen grain dispersal in still air and stationary, near homogeneous, isotropic turbulence. *Journal of Aerosol Science*, 42, 867–882.
- Scarano, F. (2013). Tomographic PIV: Principles and practice. *Measurement Science and Technology*, 24, 012001. <http://doi.org/10.1088/0957-0233/24/1/012001>.
- Scarano, F., & Poelma, C. (2009). Three-dimensional vorticity patterns of cylinder wakes. *Experiments in Fluids*, 47, 69–83. <http://doi.org/10.1007/s00348-009-0629-2>.

- Schnarrs, U., & Jueptner, W. (2005). *Digital holography*. Berlin, Heidelberg: Springer.
- Sheng, J., Malkiel, E., & Katz, J. (2009). Buffer layer structures associated with extreme wall stress events in a smooth wall turbulent boundary layer. *Journal of Fluid Mechanics*, 633, 17–60.
- Shields, A. (1936). Anwendung der Aehnlichkeitsmechanik und der Turbulenzforschung auf die Geschiebepbewegung. *Mitteilungen der Preußischen Versuchsanstalt für Wasserbau und Schiffbau*, Berlin
- Soldati, A. (2005). Particles turbulence interactions in boundary layers. *Journal of Angewandte Mathematical Mechanics*, 85, 683–699.
- Soldati, A., & Marchioli, C. (2009). Physics and modelling of turbulent particle deposition and entrainment: Review of a systematic study. *International Journal of Multiphase Flow*, 35, 827–839. <http://doi.org/10.1016/j.ijmultiphaseflow.2009.02.016>.
- Sutherland, A. J. (1967). Proposed mechanism for sediment entrainment by turbulent flows. *Journal of GeoPhysics Research*, 72, 6183–6194.
- Takemura, F., & Magnaudet, J. (2003). The transverse force on clean and contaminated bubbles rising near a vertical wall at moderate Reynolds number. *Journal of Fluid Mechanics*, 495, 235–253. <http://doi.org/10.1017/S0022112003006232>.
- van Hout, R. (2011). Time-resolved PIV measurements of the interaction of polystyrene beads with near-wall-coherent structures in a turbulent channel flow. *International Journal of Multiphase Flow*, 37(4), 346–357. <http://doi.org/10.1016/j.ijmultiphaseflow.2010.11.004>.
- van Hout, R. (2013). Spatially and temporally resolved measurements of bead resuspension and saltation in a turbulent water channel flow. *Journal of Fluid Mechanics*, 715, 389–423. <http://doi.org/10.1017/jfm.2012.525>.
- van Hout, R., Sabban, L., & Cohen, A. (2013). The use of high-speed PIV and holographic cinematography in the study of fiber suspension flows. *Acta Mechanica*, 224, 2263–2280. <http://doi.org/10.1007/s00707-013-0917-z>.
- Vikram, C. S. (1992). *Particle field holography*. Cambridge University Press.
- Westerweel, J., Elsinga, G. E., & Adrian, R. J. (2012). Particle image velocimetry for complex and turbulent flows. *Annual Review of Fluid Mechanics*, 45, 409–436. <http://doi.org/10.1146/annurev-fluid-120710-101204>.
- White, B. R., & Schulz, J. C. (1977). Magnus effect in saltation. *Journal of Fluid Mechanics*, 81, 497. <http://doi.org/10.1017/S0022112077002183>.
- White, S. J. (1970). Plane bed thresholds of fine grained sediments. *Nature*, 228, 152–153.
- Wiberg, P. L., & Smith, J. D. (1985). A theoretical model for saltating grains in water. *Journal of Geophysical Research*, 90, 7341–7354.
- Wieneke, B. (2008). Volume self-calibration for 3D particle image velocimetry. *Experiments in Fluids*, 45, 549–556. <http://doi.org/10.1007/s00348-008-0521-5>.
- Willmarth, W. W., & Lu, S. S. (1972). Structure of the Reynolds stress near the wall. *Journal of Fluid Mechanics*, 55, 65. <http://doi.org/10.1017/S002211207200165X>.
- Wu, Y., & Christensen, K. T. (2006). Population trends of spanwise vortices in wall turbulence. *Journal of Fluid Mechanics*, 568, 55. <http://doi.org/10.1017/S002211200600259X>.
- Yang, W., Kostinski, A. B., & Shaw, R. A. (2005). holography of particle fields. *Optics Letters*, 30, 1303–1305.
- Zeng, L., Balachandar, S., & Fischer, P. (2005). Wall-induced forces on a rigid sphere at finite Reynolds number. *Journal of Fluid Mechanics*, 536, 1–25. <http://doi.org/10.1017/S0022112005004738>.
- Zeng, L., Najjar, F., Balachandar, S., & Fischer, P. (2009). Forces on a finite-sized particle located close to a wall in a linear shear flow. *Physics of Fluids*, 21, 1–18. <http://doi.org/10.1063/1.3082232>.
- Zhou, J., Adrian, R. J., Balachandar, S., & Kendall, T. M. (1999). Mechanisms for generating coherent packets of hairpin vortices in channel flow. *Journal of Fluid Mechanics*, 387, 353–396. <http://doi.org/10.1017/S002211209900467X>.

Particles in Wall-Bounded Turbulent Flows: Deposition,
Re-Suspension and Agglomeration

Minier, J.-P.; Pozorski, J. (Eds.)

2017, VII, 261 p. 176 illus., 25 illus. in color., Hardcover

ISBN: 978-3-319-41566-6